

Performance of cross-polarization experiment at conditions of radiofrequency field inhomogeneity and slow to ultrafast MAS

Andrej Šmelko¹, Jan Blahut², Bernd Reif^{3,4,*}, Zdeněk Tošner^{1,*}

¹Department of Chemistry, Faculty of Science, Charles University, Albertov 6, 12842 Prague, Czech Republic

²Institute of Organic Chemistry and Biochemistry of the CAS, Flemingovo nám. 2, 16610, Prague, Czech Republic

³Bayerisches NMR Zentrum (BNMRZ) at School of Natural Sciences, Department of Bioscience, Technische Universität München (TUM), Lichtenbergstr. 4, 85747 Garching, Germany

⁴Helmholtz-Zentrum München (HMGU), Deutsches Forschungszentrum für Gesundheit und Umwelt, 85764 Neuherberg, Germany

*Corresponding authors:

- Zdeněk Tošner, zdenek.tosner@natur.cuni.cz
- Bernd Reif, reif@tum.de

Abstract

In this manuscript, we provide an analytical description of the performance of the cross-polarization experiment, including linear **rampramps** and adiabatic tangential **sweep-modifications****sweeps**, using effective Hamiltonians and simple rotations in 3D space. It is shown that radiofrequency field inhomogeneity induces a reduction of the transfer efficiency at increasing MAS frequencies for both the ramp and the adiabatic CP experiments. The effect depends on the ratio of the dipolar coupling constant and the sample rotation frequency. In particular, our simulations show that for small dipolar couplings (1 kHz) and ultrafast MAS (above 100 kHz) the transfer efficiency is below 40% when extended contact times up to 20 ms are used and relaxation losses are ignored. New recoupling and magnetization transfer techniques that are designed explicitly to account for inhomogeneous RF fields are needed.

33 1. Introduction

34 Cross polarization is a remarkable experiment with a very long history (Schaefer, 2007). In 1962,
35 Hartmann and Hahn (Hartmann and Hahn, 1962) presented the theory of magnetization transfer in a
36 two-spin system under conditions of double radiofrequency (RF) irradiation of a static sample. In 1973,
37 Pines et al. (Pines et al., 1973) published their seminal work on proton-enhanced solid-state NMR of
38 dilute spins such as ^{13}C and ^{15}N . While magic angle spinning (MAS) was introduced by Andrew et al.
39 (ANDREW et al., 1958) and independently by Lowe (Lowe, 1959) already in 1958 and 1959,
40 respectively, it was only in 1977 that cross polarization was successfully combined with sample
41 rotation. The necessary modification of the Hartmann-Hahn conditions was described by Stejskal et al.
42 (Stejskal et al., 1977). After that, many modifications with variable amplitude irradiations on one or
43 both RF channels were developed. Among them, simple linear ramps (Metz et al., 1994) and adiabatic
44 sweeps (Hediger et al., 1995) became most popular. Ramp-CP was originally introduced to broaden
45 the Hartmann-Hahn (HH) matching condition and to obtain uniform signal amplitudes. In the original
46 publication, low MAS frequencies (below ~ 10 kHz) were used and the sweep could cover several HH
47 conditions. At the same time, it was realized that the largest enhancement in signal intensity is
48 obtained when the sweep covers only one HH condition (Metz et al., 1994). The RF amplitude sweep
49 implies a partially adiabatic inversion of the spins and compensates RF field inhomogeneities (Peersen
50 et al., 1994; Hediger et al., 1995).

51 Until now, cross-polarization remains the main pulse sequence building block for magnetization
52 transfers. At very high MAS frequencies, it becomes difficult to achieve HH zero-quantum matching
53 where the difference of the two applied rf amplitudes is equal to the MAS frequency. Instead, the HH
54 double-quantum matching condition must be used in which the sum of the RF amplitudes equals the
55 MAS frequency. The spin dynamics remains the same with the exception that negative intensities are
56 obtained ~~(Meier, 1992)~~. Cross-polarization is thus applied over an exceptionally wide range of
57 conditions, from experiments using static samples to MAS experiments with rotation frequencies
58 above 100 kHz.

~~59 Developments in NMR hardware and pulse sequences are largely driven by biomolecular
60 applications. Due to difficulties in sample preparation, only limited amounts of material are available
61 that do not allow to completely fill the MAS rotor. It has been noticed that restriction of the sample
62 volume to 30% with aligning the sample in the center of the solenoidal coil does not lead to a
63 substantial reduction in sensitivity in ^{15}N , ^{13}C correlation experiments. This volume selective behavior
64 of the cross-polarization experiment is due to the inhomogeneous radiofrequency (RF) field
65 distribution generated by the solenoidal coil. Although the RF field is rather homogeneous in the
66 central area of the rotor, it quickly decays towards the end of the coil and cross-polarization
67 mediated polarization transfer is impaired due to mismatch of RF amplitudes. The limited availability
68 of biological sample and the use of center packed rotors are presumably the reason why the
69 detrimental effects of RF field inhomogeneity were neglected in the development of new solid-state
70 NMR experiments for so long. The rotors for ultrafast MAS, however, The most widespread coil
71 design used by all vendors in most of the MAS solid-state NMR probes is a solenoid. Its simple design,
72 large filling factor, high conversion ratio from RF power to RF field, and its possibility to be integrated
73 into circuits tuned to multiple frequencies are among the major benefits. The main drawback is its~~

74 inhomogeneous RF field, which quickly decays towards the end of the coil, where the RF amplitude is
75 reduced to about 50% of the value achieved in the coil center. Several other strategies have been
76 proposed to design NMR coils that are compatible with MAS and provide improved RF field
77 homogeneity. Variable pitch coils were proposed by Idziak and Haeberlen (Idziak and Haeberlen,
78 1982) and recently explored by Martin et al. (Kelz et al., 2019), who proposed 3D-printed templates
79 for easy manufacturing. An interesting alternative was proposed by Privalov et al. (Privalov et al.,
80 1996) using variable ribbon width coils that improve RF homogeneity not only along the coil axis but
81 also in the radial direction. Another type of coil was designed for so-called E-free probes, which
82 minimize sample heating effects induced by high-power RF irradiation. These coils also show
83 improved RF field homogeneity (Krahn et al., 2008). All strategies have benefits and disadvantages.
84 Variable-pitch coils provide a lower RF conversion ratio and thus lower sensitivity. E-free probes
85 consist of separated coils for the high- and low-frequency RF channels, which potentially leads to
86 different RF field profiles and imbalances between these channels. Worth mentioning is the recent
87 cryo CP-MAS probe technology that is reported to provide excellent RF field homogeneity (Hassan et
88 al., 2020).

89 RF field inhomogeneity is a concern for the performance of virtually all NMR experiments. Specifically,
90 it affects the sensitivity of the cross-polarization experiment, since the Hartmann-Hahn matching is
91 violated at different positions within the sample as a consequence of the modulation of the RF
92 amplitudes due to inhomogeneity. An experimental example of this volume-selective behavior of the
93 cross-polarization experiment is presented, for example, in the work of Tošner et al. (Tošner et al.,
94 2018). In biomolecular applications, it is difficult to prepare large quantities of isotopically labelled
95 samples, and only limited amounts of material are available that do not allow to completely fill the
96 MAS rotor. To yield the highest possible sensitivity, samples are typically center packed around the
97 center of the coil, and the problem of RF field distribution is reduced. However, the rotors for ultrafast
98 MAS are small and can be completely filled with sample. Under these conditions, RF inhomogeneity
99 comes up as a concern- in its full range. With faster MAS and correspondingly smaller rotors that
100 contain less material, we are again facing ~~again~~-sensitivity issues. It is obviously desirable that the
101 whole sample contributes to the NMR signal. At this point, it appears that the inhomogeneity of the
102 RF field is the prevailing challenge for the development of new solid-state NMR methods.

103 In this tutorial article, we summarize the principles of the cross polarization (CP) experiment and focus
104 on the effect of RF field inhomogeneity. For demonstration purposes we limit our treatment to an
105 isolated heteronuclear pair of spin-1/2 nuclei that are coupled via the dipole-dipole interaction. We
106 assume that there is no chemical shift interaction. Using average Hamiltonian theory and simple 3D
107 rotations we explain the process of magnetization transfer assuming different amplitude swept CP
108 variants. We show that the total signal measured after the CP transfer decreases with increasing MAS
109 frequency. The effect is amplified for small dipolar couplings. We numerically optimize linear ramp and
110 adiabatic tangential sweep experiments to identify the conditions for the best performance as a
111 function of the dipolar coupling constant, contact time, and MAS frequency. Neither of these
112 techniques under any condition fully compensates for RF field inhomogeneities. The most striking
113 example of low efficiency is the CP transfer between a ¹⁵N nucleus directly bonded to a ¹³C atom
114 involving a dipolar coupling constant of about 1 kHz. With the forthcoming MAS technology in mind
115 that can reach MAS frequencies of up to 200 kHz, we predict that only 20% of the sample will

116 contribute to the NMR signal after a CP mixing time of 10 ms. It clearly calls for the development of
 117 alternative magnetization transfer techniques that are suitable for ultrafast MAS NMR experiments.

118

119 2. Theory

120 A theoretical description of the cross polarization phenomenon can be found in many solid-state NMR
 121 textbooks. Here, we revisit the relevant parts and focus on visualization of the magnetization transfer
 122 process during variable-amplitude sequences, following the description presented by Rovnyak
 123 (Rovnyak, 2008). In the following, we assume an isolated spin pair. A more general description that
 124 considers the surrounding spins [and homonuclear interactions within an \$I_N S\$ spin system](#) can be found,
 125 for example, in the work of Vega [and coworkers \(Marks and Vega, 1996; et al. \(Ray et al., 1998\). This](#)
 126 [issue has been reviewed in the context of ultrafast MAS by Emsley and coworkers \(Laage et al., 2009\),](#)
 127 [concluding that the perturbation effects of homonuclear interactions diminish with increasing spinning](#)
 128 [rate. The authors infer that the behavior of the CP experiment at very fast spinning in a \$I_N S\$ spin system](#)
 129 [is reminiscent of a \$^{13}\text{C}\$ - \$^{15}\text{N}\$ spin pair, which we would like to analyze in the following in detail.](#)

130 2.1. Hamiltonian decomposition into ZQ and DQ subspaces

131 We start with the Hamiltonian that contains the dipole-dipole interaction and the radiofrequency fields
 132 with amplitudes ω_I and ω_S applied on resonance to spins I and S , respectively.

$$H = \omega_I I_x + \omega_S S_x + d_{IS}(t) 2I_z S_z \quad (1)$$

133 The dipolar term is time dependent due to magic angle spinning (angular frequency ω_R) and can be
 134 expressed as

$$d_{IS}(t) = g_1 \cos(\omega_R t + \gamma) + g_2 \cos(2\omega_R t + 2\gamma) \quad (2)$$

$$g_1 = -\frac{1}{\sqrt{2}} 2\pi b_{IS} \sin 2\beta \quad (3)$$

$$g_2 = \frac{1}{2} 2\pi b_{IS} \sin^2 \beta \quad (4)$$

135 where b_{IS} is the dipolar coupling constant ($b_{IS} = -\frac{\mu}{4\pi} \frac{\gamma_I \gamma_S}{r_{IS}^3} \frac{\gamma_I \gamma_S \hbar}{r_{IS}^3} \frac{1}{2\pi}$) in units of Hertz, and β, γ are the
 136 Euler angles relating the orientation of the dipolar vector \vec{r}_{IS} with the rotor axis (the α angle is
 137 irrelevant as the dipolar coupling tensor has a vanishing asymmetry).

138 Subsequently, the reference frame is transformed into the tilted frame where the radiofrequency
 139 fields are linear with I_z and S_z , while the dipolar term becomes transversal. This transformation is
 140 represented by a $\pi/2$ -rotation around $(I_y + S_y)$ and we obtain

$$H' = \omega_I I_z + \omega_S S_z + d_{IS}(t) 2I_x S_x \quad (5)$$

141 This form of the Hamiltonian allows decomposition of the spin dynamics problem into two separate
 142 subspaces, the zero quantum (ZQ) and the double quantum (DQ) subspace. The ZQ and DQ subspaces
 143 can be represented using fictitious spin-1/2 operators that are defined in Table 1.

144

145 **Table 1.** Fictitious spin-1/2 operators in zero quantum and double quantum subspaces.

Zero quantum	Double quantum
$I_x^{ZQ} = I_x S_x + I_y S_y$ $I_y^{ZQ} = I_y S_x - I_x S_y$ $I_z^{ZQ} = \frac{1}{2}(I_z - S_z)$	$I_x^{DQ} = I_x S_x - I_y S_y$ $I_y^{DQ} = I_y S_x + I_x S_y$ $I_z^{DQ} = \frac{1}{2}(I_z + S_z)$
<p data-bbox="204 495 416 524">Inverted relations</p> $I_z = I_z^{DQ} + I_z^{ZQ}$ $S_z = I_z^{DQ} - I_z^{ZQ}$ $2I_x S_x = I_x^{DQ} + I_x^{ZQ}$	

146

147 The Hamiltonian can then be written as

$$H' = H^{ZQ} + H^{DQ} \quad (6)$$

$$H^{ZQ} = (\omega_I - \omega_S)I_z^{ZQ} + d_{IS}(t)I_x^{ZQ} \quad (7)$$

$$H^{DQ} = (\omega_I + \omega_S)I_z^{DQ} + d_{IS}(t)I_x^{DQ} \quad (8)$$

148

149 **2.2. Magnetization transfer in static CP experiment**

150 The magnetization transfer process in the tilted frame is described by a transition from I_z into S_z . The
 151 action of RF pulses and the dipolar interaction on the spin state I_z in the tilted frame is evaluated
 152 independently in the ZQ and DQ subspace, working with the initial spin states I_z^{ZQ} and I_z^{DQ} ,
 153 respectively. If the sample is static, the zero-quantum Hartmann-Hahn condition is $\omega_I - \omega_S = 0$ and
 154 the Hamiltonian in Eq. (7) reduces to $H^{ZQ} = d_{IS}I_x^{ZQ}$ (d_{IS} is time independent). The spin state
 155 represented by the operator I_z^{ZQ} is rotated around the I_x^{ZQ} axis as a consequence of the dipolar
 156 interaction. Simultaneously, the spin state I_z^{DQ} evolves in the DQ subspace. We can assume that $\omega_I +$
 157 ω_S is much larger than d_{IS} . The effective rotation axis is thus oriented along I_z^{DQ} , see Eq. (8). As a result,
 158 H^{DQ} has no effect on the I_z^{DQ} state. This is summarized in the following equations.

$$I_z^{ZQ} \xrightarrow{H^{ZQ}} I_z^{ZQ} \cos d_{IS}t - I_y^{ZQ} \sin d_{IS}t$$

$$= \frac{1}{2}(I_z - S_z) \cos d_{IS}t - (I_y S_x - I_x S_y) \sin d_{IS}t \quad (9)$$

$$I_z^{DQ} \xrightarrow{H^{DQ}} I_z^{DQ} = \frac{1}{2}(I_z + S_z) \quad (10)$$

$$I_z = I_z^{ZQ} + I_z^{DQ} \xrightarrow{H^{ZQ}+H^{DQ}} I_z \frac{1}{2}(\cos d_{IS}t + 1) + S_z \frac{1}{2}(1 - \cos d_{IS}t)$$

$$- (I_y S_x - I_x S_y) \sin d_{IS}t \quad (11)$$

159

160 The I_z spin state is transformed into S_z when $\cos d_{IS}t = -1$, resulting in a full inversion of the I_z^{ZQ}
 161 operator.

162 For the double-quantum Hartmann-Hahn condition $\omega_I + \omega_S = 0$, the rotation occurs in the DQ
 163 subspace. In analogy to the previous case, we assume $|\omega_I - \omega_S| \gg d_{IS}$. Under this precondition, the
 164 ZQ spin state is not changed.

$$I_z^{ZQ} \xrightarrow{H^{ZQ}} I_z^{ZQ} = \frac{1}{2}(I_z - S_z) \quad (12)$$

$$\begin{aligned} I_z^{DQ} &\xrightarrow{H^{DQ}} I_z^{DQ} \cos d_{IS}t - I_y^{DQ} \sin d_{IS}t \\ &= \frac{1}{2}(I_z + S_z) \cos d_{IS}t - (I_y S_x + I_x S_y) \sin d_{IS}t \end{aligned} \quad (13)$$

$$\begin{aligned} I_z = I_z^{ZQ} + I_z^{DQ} &\xrightarrow{H^{ZQ} + H^{DQ}} I_z \frac{1}{2}(\cos d_{IS}t + 1) - S_z \frac{1}{2}(1 - \cos d_{IS}t) \\ &\quad - (I_y S_x + I_x S_y) \sin d_{IS}t \end{aligned} \quad (14)$$

165 For $\cos d_{IS}t = -1$, the I_z^{DQ} operator is inverted resulting in generation of the operator $-S_z$. Note that
 166 the double quantum Hartmann-Hahn condition yields negative signal intensity.

167 The dipolar coupling is an orientation dependent interaction. ~~The above derived results describe the~~
 168 ~~matching conditions for a particular crystallite orientation.~~ To yield the magnetization transfer
 169 dynamics for a powder sample, the ensemble of all possible crystallite orientations has to be accounted
 170 for. The powder averaged inversion efficiency is lower since the condition of a complete transfer,
 171 $\cos d_{IS}t = -1$, will hold only for a single orientation.

172 **2.3. Magic angle spinning and average Hamiltonians**

173 In case of MAS, the Hamiltonians become time dependent. The analysis is performed then using
 174 average Hamiltonian theory (AHT) employing the Magnus expansion. A tutorial on AHT principles was
 175 presented by Brinkmann (Brinkmann, 2016). To retain fast convergence of the Magnus series, the
 176 Hamiltonian is expressed in an appropriate interaction frame. Eq. (2) implies four resonance conditions
 177 upon transformation into a new rotating frame in which the periodic modulations of $d_{IS}(t)$ are
 178 removed by application of RF fields. These resonance conditions are associated with the characteristic
 179 frequencies $n\omega_R$ with $n = \pm 1, \pm 2$. We choose $n = +1$ and focus on the ZQ subspace. In general,
 180 transformation to a new reference frame is described using a propagator $U_T(t)$. This propagator
 181 transforms the Hamiltonian according to

$$H' = U_T^\dagger(t) H U_T(t) - i U_T^\dagger(t) \frac{d}{dt} U_T(t) \quad (15)$$

182 In this case, $U_T(t) = \exp(-i\omega_R t I_z^{ZQ})$. The transformation can be regarded as a rotation around I_z^{ZQ}
 183 with a frequency $-\omega_R$. The second term in Eq. (15) is a Coriolis term which introduces the term
 184 $-\omega_R I_z^{ZQ}$ into the transformed Hamiltonian.

$$H^{ZQ'} = (\omega_I - \omega_S - \omega_R) I_z^{ZQ} + d_{IS}(t) (I_x^{ZQ} \cos \omega_R t - I_y^{ZQ} \sin \omega_R t) \quad (16)$$

185 The first order Hamiltonian is the time average over the modulation period $\tau_R = 2\pi/\omega_R$,

$$\bar{H}^{ZQ} = \frac{1}{\tau_R} \int_0^{\tau_R} H^{ZQ'} dt \quad (17)$$

186 The integral over the time dependent parts in Eq. (16) is evaluated as follows (making use of
 187 [goniometrietrigonometric](#) identities)

$$\begin{aligned}
 188 \quad & \frac{1}{\tau_R} \int_0^{\tau_R} [g_1 \cos(\omega_R t + \gamma) + g_2 \cos(2\omega_R t + 2\gamma)] (I_x^{ZQ} \cos \omega_R t - I_y^{ZQ} \sin \omega_R t) dt = \\
 189 \quad & = \frac{1}{\tau_R} \int_0^{\tau_r} \left\{ g_1 \frac{1}{2} [\cos(2\omega_R t + \gamma) + \cos \gamma] + g_2 \frac{1}{2} [\cos(3\omega_R t + 2\gamma) + \cos(\omega_R t + 2\gamma)] \right\} dt I_x^{ZQ} + \\
 190 \quad & - \frac{1}{\tau_R} \int_0^{\tau_r} \left\{ g_1 \frac{1}{2} [\sin(2\omega_R t + \gamma) - \sin \gamma] + g_2 \frac{1}{2} [\sin(3\omega_R t + 2\gamma) - \sin(\omega_R t + 2\gamma)] \right\} dt I_y^{ZQ} = \\
 191 \quad & = \frac{1}{2} g_1 \cos \gamma I_x^{ZQ} + \frac{1}{2} g_1 \sin \gamma I_y^{ZQ}
 \end{aligned}$$

192 We obtain the first order average Hamiltonian in the ZQ subspace thus as

$$\bar{H}^{ZQ} = (\omega_I - \omega_S - \omega_R) I_z^{ZQ} + \frac{1}{2} g_1 (\cos \gamma I_x^{ZQ} + \sin \gamma I_y^{ZQ}) \quad (18)$$

193 The Hartmann-Hahn condition is corrected to account for the rotation of the sample and has the form
 194 $\omega_I - \omega_S = \omega_R$. In this case, the component of \bar{H}^{ZQ} along the I_z^{ZQ} axis is zero and the dipolar
 195 interaction results in a rotation around an axis in the transversal plane, with a phase depending on γ .
 196 For each crystallite, the spin state I_z^{ZQ} is flipped away from the z axis generating a transversal
 197 component. These transversal components are equally distributed with respect to the γ angle and
 198 average to zero in a powder sample. Only the projection on the I_z^{ZQ} axis is relevant, and we can
 199 therefore arbitrarily set $\gamma = 0$.

200 The calculation can be repeated for other choices of n and the following zero-quantum average
 201 Hamiltonians are obtained

$$\bar{H}^{ZQ} = (\omega_I - \omega_S - n\omega_R) I_z^{ZQ} + \frac{1}{2} g_n I_x^{ZQ} \quad (19)$$

202 The fast convergence of the Magnus expansion is maintained and the proper description of spin
 203 dynamics by an average Hamiltonian is valid in the vicinity of the Hartmann-Hahn condition ($\omega_I - \omega_S -$
 204 $n\omega_R = 0$). The RF amplitudes ω_I and ω_S may become time dependent in case a linear ramp or an
 205 adiabatic sweep is applied. In any case, we assume that RF changes are slow compared to the MAS
 206 frequency to ensure validity of this treatment.

207 The analysis is completed by inspecting the spin dynamics in the DQ subspace. We apply the same
 208 procedure as for the ZQ subspace, yielding

$$\bar{H}^{DQ} = (\omega_I + \omega_S - n\omega_R) I_z^{DQ} + \frac{1}{2} g_n I_x^{DQ} \quad (20)$$

209 For the zero quantum condition, it is assumed that the I_z^{DQ} term dominates the average Hamiltonian
 210 \bar{H}^{DQ} , i.e. $\omega_I + \omega_S - n\omega_R \gg d_{IS}$ for all $n = \pm 1, \pm 2$. Under these conditions, the initial state I_z^{DQ}

211 remains unchanged. However, these conditions might be violated for large RF amplitude sweeps or in
 212 case of substantial RF field inhomogeneity.

213 **2.4. CP matching profiles**

214 For constant RF amplitudes, the magnetization transfer process can be analytically described to derive
 215 the so-called CP matching profiles (sometimes dubbed Hartmann-Hahn fingers). This derivation was
 216 previously published by Levitt (Levitt, 1991), and Wu and Zilm (Wu and Zilm, 1993). It is assumed that
 217 both the ZQ and DQ Hartmann-Hahn conditions are independent. We reiterate the calculation for the
 218 matching condition and focus first on the ZQ Hamiltonian given in Eq. (19). We proceed with the final
 219 transformation into the effective field of the Hamiltonian. The Hamiltonian \bar{H}^{ZQ} can be represented
 220 as a vector in the xz plane. This vector has an angle ϕ with the x axis. The transformation into the
 221 effective field is described by a rotation around I_y^{ZQ} by an angle $-\phi$, which is equivalent to the
 222 application of the propagator $U_T = \exp(-i\phi I_y^{ZQ})$. It makes the x axis of the new frame to coincide
 223 with the effective Hamiltonian vector. Note that the Coriolis term in Eq. (15) is zero because U_T is time
 224 independent. The effective Hamiltonian can be written as

$$\bar{H}_{eff}^{ZQ} = \omega_{eff}^{ZQ,n} I_x^{eff} \quad (21)$$

$$\omega_{eff}^{ZQ,n} = \sqrt{(\omega_I - \omega_S - n\omega_R)^2 + \frac{1}{4}g_n^2} \quad (22)$$

$$\tan \phi = \frac{\omega_I - \omega_S - n\omega_R}{\frac{1}{2}g_n} \quad (23)$$

225 The initial spin state $\rho^{ZQ}(0) = I_z^{ZQ}$ transforms into $\rho^{eff}(0) = U_T^\dagger \rho^{ZQ}(0) U_T = \cos \phi I_z^{eff} +$
 226 $\sin \phi I_x^{eff}$ in the effective field frame, and evolves with a frequency $\omega_{eff}^{ZQ,n}$ around the effective field
 227 axis I_x^{eff}

$$\begin{aligned} \rho^{eff}(t) &= \cos \phi (I_z^{eff} \cos \omega_{eff}^{ZQ,n} t - I_y^{eff} \sin \omega_{eff}^{ZQ,n} t) + \sin \phi I_x^{eff} \\ &= \sin \phi I_x^{eff} - \cos \phi \sin \omega_{eff}^{ZQ,n} t I_y^{eff} + \cos \phi \cos \omega_{eff}^{ZQ,n} t I_z^{eff} \end{aligned} \quad (24)$$

228 The result is transformed back from the effective field frame into the ZQ subspace as $\rho^{ZQ}(t) =$
 229 $U_T \rho^{eff}(t) U_T^\dagger$. This yields

$$\begin{aligned} \rho^{ZQ}(t) &= \sin \phi (I_x^{ZQ} \cos \phi + I_z^{ZQ} \sin \phi) - \cos \phi \sin \omega_{eff}^{ZQ,n} t I_y^{ZQ} \\ &\quad + \cos \phi \cos \omega_{eff}^{ZQ,n} t (I_z^{ZQ} \cos \phi - I_x^{ZQ} \sin \phi) \\ &= \sin \phi \cos \phi (1 - \cos \omega_{eff}^{ZQ,n} t) I_x^{ZQ} - \cos \phi \sin \omega_{eff}^{ZQ,n} t I_y^{ZQ} \\ &\quad + (\sin^2 \phi + \cos^2 \phi \cos \omega_{eff}^{ZQ,n} t) I_z^{ZQ} \end{aligned} \quad (25)$$

230 Eq. (25) describes the trajectory of the I_z^{ZQ} operator in the ZQ subspace under the influence of the RF
 231 pulses applied in the CP experiment. For evaluation of the magnetization transfer process, only the
 232 projection on the I_z^{ZQ} axis is important. We assume that there is no evolution in the DQ subspace, i.e.
 233 $\rho^{DQ}(t) = I_z^{DQ}$. The initial I_z operator thus evolves as (recall $I_z = I_z^{ZQ} + I_z^{DQ}$)

$$\rho^{ZQ}(t) + \rho^{DQ}(t) = (\sin^2 \phi + \cos^2 \phi \cos \omega_{eff}^{ZQ,n} t) \frac{1}{2} (I_z - S_z) + \frac{1}{2} (I_z + S_z) \quad (26)$$

234 We obtain the CP transfer efficiency in the vicinity of the zero quantum condition (n) by collecting the
235 terms in front of the S_z operator

$$\begin{aligned} \epsilon^{ZQ,n} &= \frac{1}{2} (1 - \sin^2 \phi - \cos^2 \phi \cos \omega_{eff}^{ZQ,n} t) = \frac{1}{2} (\cos^2 \phi - \cos^2 \phi \cos \omega_{eff}^{ZQ,n} t) \\ &= \frac{\cos^2 \phi}{2} (1 - \cos \omega_{eff}^{ZQ,n} t) \\ \epsilon^{ZQ,n} &= \frac{1}{2} \frac{\frac{1}{4} g_n^2}{(\omega_I - \omega_S - n\omega_R)^2 + \frac{1}{4} g_n^2} [1 - \cos \omega_{eff}^{ZQ,n} t] \end{aligned} \quad (27)$$

236 A similar calculation for the double quantum Hartmann-Hahn condition yields

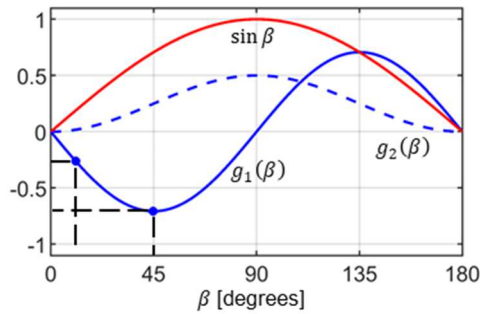
$$\epsilon^{DQ,n} = -\frac{1}{2} \frac{\frac{1}{4} g_n^2}{(\omega_I + \omega_S - n\omega_R)^2 + \frac{1}{4} g_n^2} [1 - \cos \omega_{eff}^{DQ,n} t] \quad (28)$$

$$\omega_{eff}^{DQ,n} = \sqrt{(\omega_I + \omega_S - n\omega_R)^2 + \frac{1}{4} g_n^2} \quad (29)$$

237 Note the negative sign of the transferred magnetization for the double quantum Hartmann-Hahn
238 transfer. Equations (27) and (28) are identical to the result of an alternative derivation presented by
239 Marica and Snider (Marica and Snider, 2003). The CP MAS matching profile has the form of a Lorentzian
240 function with a width that is dependent on the dipolar coupling b_{IS} and the crystallite orientation
241 (Euler angle β), that are included in the g_n factors. In powders, a quantitative magnetization transfer
242 is not possible as a consequence of the dependence of the size of the effective dipolar coupling on
243 orientation. The magnetization transfer efficiency under MAS is independent of the γ angle. This
244 property is referred to as γ -encoding. The powder average is obtained by evaluation of the integral

$$\langle \epsilon^{ZQ,n} \rangle_{powder} = \frac{1}{2} \int_0^\pi \epsilon^{ZQ,n} \sin \beta d\beta \quad (30)$$

245



246

247 **Figure 1.** Dipolar coupling scaling factors $g_1(\beta)$ (solid blue line) and $g_2(\beta)$ (dashed blue line) defined
248 in Eqs. (3), (4). The red curve represents the relative probability to find a specific orientation in a

249 powder sample. This weighting factor is employed for the calculation of the transfer efficiencies ϵ in
 250 Eq. (30). β angles with $\beta=15^\circ$ and 45° are used for the visualization of the spin dynamics in the
 251 Discussion.

252

253 **2.5. Radiofrequency field inhomogeneity**

254 Radiofrequency fields in MAS probes are realized using solenoid coils. However, a solenoid produces a
 255 rather inhomogeneous distribution of magnetic fields across the sample (Tosner et al., 2017).
 256 Moreover, as the sample rotates, individual spin packets travel along circles through a spatially
 257 inhomogeneous RF field which is determined by the helical geometry of the solenoid coil. This RF
 258 inhomogeneity introduces periodic modulations of both the RF amplitude and phase. For the special
 259 case of the CP experiment, it was recently shown that these temporal modulations have a negligible
 260 effect (Aebischer et al., 2021) and will be ignored in the present treatment. In addition, the distribution
 261 of the RF fields depends on the frequency (Engelke, 2002), and can be influenced by different balancing
 262 of the RF circuitry on different channels (Paulson et al., 2004). For simplicity, we assume the RF field
 263 distributions to be equal for the I and S spins and disregard the radial dependency. The effect of RF
 264 field inhomogeneity on the CP experiment was previously studied by Paulson et al. (Paulson et al.,
 265 2004), and Gupta et al. (Gupta et al., 2015). An example of the distribution of the RF field along the
 266 coil axis, denoted $\xi(z)$, is shown in Figure 2. As noted by Gupta et al., the profile deviates from a
 267 Gaussian function and is well described by a power law dependence. In our study, we use the B_1 profile
 268 calculated according to Engelke (Engelke, 2002).

269 The distribution of RF field amplitudes enters the formulas of the CP experiment using the substitution

$$\begin{aligned} \omega_I &\xrightarrow{\text{replace}} \xi(z)\omega_I^{NOM} \\ \omega_S &\xrightarrow{\text{replace}} \xi(z)\omega_S^{NOM} \end{aligned} \quad (31)$$

270 where ω_I^{NOM} , ω_S^{NOM} refer to the nominal RF amplitudes realized in the center of the coil ($z = 0$ where
 271 $\xi(0) = 1$). The overall experimental efficiency corresponds to the integral over the sample volume
 272 weighted by the detection sensitivity of the coil. According to the reciprocity theorem (Hoult, 2000),
 273 the sensitivity is proportional to the RF field. We assume that the sample extends over a length l , and
 274 is placed symmetrically within the solenoid coil.

$$\langle \epsilon^{ZQ,n} \rangle_{\text{powder}}^{rf-inh} = \frac{1}{w} \int_{-l/2}^{+l/2} \langle \epsilon^{ZQ,n} \rangle_{\text{powder}} \xi(z) dz \quad (32)$$

275 The normalization factor w is given as

$$w = \int_{-l/2}^{+l/2} \xi(z) dz \quad (33)$$

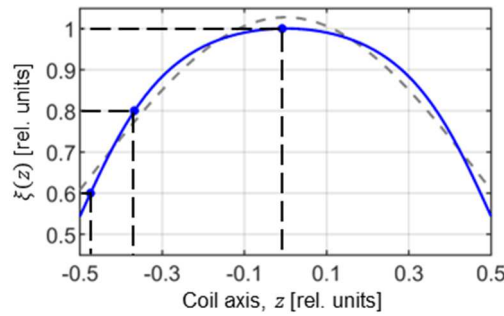
276 It is not possible to match the Hartmann-Hahn conditions for the whole sample volume. Assuming that
 277 the zero-quantum condition is fulfilled for the nominal rf amplitudes, i.e., $\omega_I^{NOM} - \omega_S^{NOM} = n\omega_R$, we
 278 get

$$\omega_I - \omega_S - n\omega_R = \xi(z)(\omega_I^{NOM} - \omega_S^{NOM}) - n\omega_R = \xi(z)n\omega_R - n\omega_R = n\omega_R(\xi(z) - 1)$$

280 and

$$\bar{H}^{ZQ} = n\omega_R[\xi(z) - 1]I_z^{ZQ} + \frac{1}{2}g_n I_x^{ZQ} \quad (34)$$

281 Eq. (34) shows that in the case of an inhomogeneous RF field, the prevailing component along the I_z^{ZQ}
 282 operator in the effective Hamiltonian \bar{H}^{ZQ} is proportional to the MAS frequency ω_R , multiplied by the
 283 order of the recoupling condition n . The effect of RF amplitude mismatch on spin dynamics is more
 284 pronounced for small dipolar couplings, b_{IS} , which is reflected in the width of the CP MAS matching
 285 profiles derived above. Thus, we could analytically derive a dependence of the performance of the CP
 286 experiment on the MAS frequency.



287

288 **Figure 2:** RF field inhomogeneity profile along the axis of a solenoid coil. The profile is calculated
 289 according to Engelke (Engelke, 2002) assuming a coil length of 7.9 mm, a diameter of 3.95 mm, and
 290 assuming 7 turns (blue line). The grey dashed line represents a fit of the RF profile assuming a Gaussian
 291 function suggested by Paulson et al. (Paulson et al., 2004). The power law relation introduced by Gupta
 292 et al. (Gupta et al., 2015) yields a perfect fit of the theoretical behavior and exactly matches the blue
 293 curve. Values $\xi=0.6, 0.8$, and 1.0 are used in the Discussion session to visualize spin dynamics.

294

295 **2.6. Linear ramp and adiabatic sweep**

296 The most popular way to overcome the limitations of the constant amplitude CP and the RF mismatch
 297 at different positions of the sample is the use of a linear ramp or an adiabatic tangential sweep on one
 298 of the RF channels. We can define

$$\omega_I^{NOM} = \omega_I^0 + f(t) \quad (35)$$

299 where the function $f(t)$ describes the sweep from $-\Delta/2$ to $+\Delta/2$ over time $t \in \langle 0, T \rangle$. The function
 300 $f(t)$ can be defined for the linear ramp as

$$f(t) = \Delta \left(\frac{t}{T} - \frac{1}{2} \right) \quad (36)$$

301 and for tangential sweep as

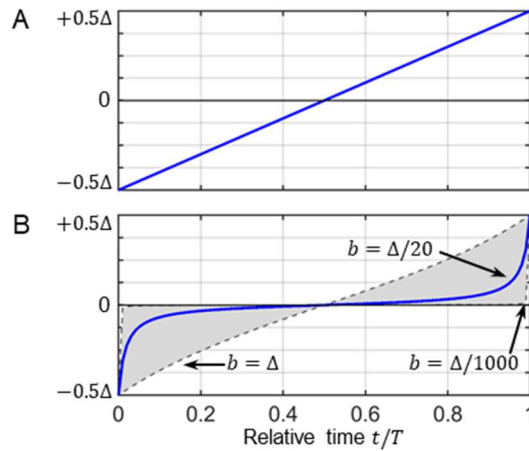
$$f(t) = b \tan \left[\left(\frac{2t}{T} - 1 \right) \arctan \frac{\Delta}{2b} \right] \quad (37)$$

302 where b parametrizes the curvature of the sweep. Values for b are typically in the range of $\frac{\Delta}{1000} < b <$
 303 Δ . For $b = \frac{\Delta}{1000}$, $f(t)$ is almost constant except for the end points where the function rapidly changes
 304 from/to $\mp\Delta/2$. For $b = \Delta$, $f(t)$ approaches the linear ramp. The influence of b on the shape is
 305 illustrated in Figure 3. During a truly adiabatic transfer, the effective field is aligned with the initial
 306 magnetization along the $+I_z^{ZQ}$ axis, and changes its orientation slowly towards $-I_z^{ZQ}$. The spin state is
 307 locked along the effective field and is inverted as well (Hediger et al., 1995). The adiabaticity condition
 308 is given as

$$\frac{d}{dt}\phi(t) \ll \omega_{eff} \quad (38)$$

309 where ω_{eff} is defined in Eq. (22), and the angle ϕ is given in Eq. (23). Adiabatic inversion pulses have
 310 been an integral part of the NMR toolbox for a long time (Baum et al., 1985). There is, however, a
 311 substantial difference between broadband inversion pulses and cross-polarization. Inversion pulses
 312 allow to manipulate the effective field along both z and x directions, corresponding to offset and RF
 313 amplitude, respectively. In the CP experiment, the x axis component of the effective Hamiltonian is
 314 fixed and is determined by the dipolar coupling, see Eq. (19) and Eq. (20). In addition, perfect alignment
 315 of the effective field with the initial state is difficult to achieve as the RF amplitudes are restricted to
 316 the vicinity of the Hartmann-Hahn condition.

317



318

319 **Figure 3:** RF amplitude sweeps employed in cross-polarization experiments for (A) a linear ramp and
 320 (B) an adiabatic tangential sweep. Eq. (36) and (37) mathematically describe the time dependent RF
 321 amplitude. The parameter b determines the curvature of the adiabatic tangential shape.

322

323 **2.7. RF amplitude sweeps and RF field inhomogeneity**

324 In the following, we aim to include RF field inhomogeneity in the description of the RF amplitude sweep
 325 of Eq. (35). We assume that the zero quantum Hartmann-Hahn matching conditions are fulfilled in the
 326 middle of the sweep and in the center of the coil for the nominal RF field amplitudes, i.e. for $\omega_I^0 -$
 327 $\omega_S^{NOM} = n\omega_R$. The I_z^{ZQ} component of the Hamiltonian \bar{H}^{ZQ} then becomes

$$\begin{aligned}
\omega_I - \omega_S - n\omega_R &= \xi(z)[\omega_I^{NOM} - \omega_S^{NOM}] - n\omega_R \\
&= \xi(z)[\omega_I^0 + f(t) - \omega_S^{NOM}] - n\omega_R = \xi(z)[f(t) + n\omega_R] - n\omega_R \quad (39) \\
&= \xi(z)f(t) + n\omega_R[\xi(z) - 1]
\end{aligned}$$

328 and

$$\bar{H}^{ZQ} = \{\xi(z)f(t) + n\omega_R[\xi(z) - 1]\}I_z^{ZQ} + \frac{1}{2}g_n I_x^{ZQ} \quad (40)$$

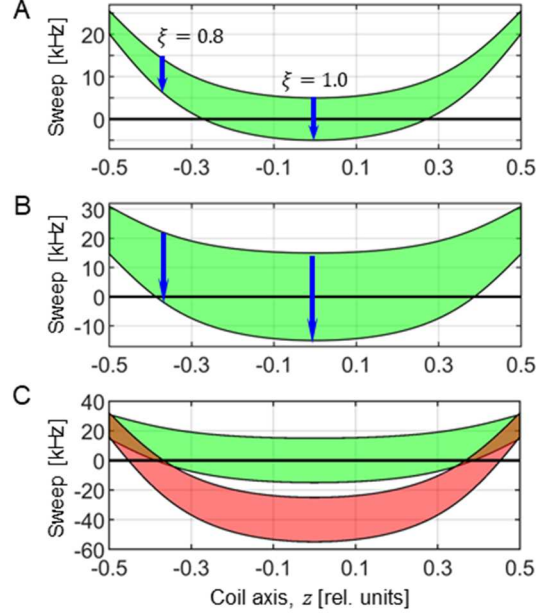
329 Now, the sweep function $f(t)$ is scaled by the RF field inhomogeneity factor $\xi(z)$. At the same time,
330 the center of the sweep is shifted by an amount proportional to the MAS frequency ω_R . In Figure 4,
331 the sweep range is depicted in green as a function of position along the coil axis. Spins located in
332 volume elements towards the ends of the coil where the RF field is smaller experience RF amplitude
333 sweeps that do not cover the recoupling condition at all (e.g. for $\xi=0.8$ in Figure 4A). This is another
334 example of how increased MAS frequencies impact the cross-polarization experiment and cause a
335 decrease in performance.

336 When setting the numerical values of RF amplitudes ω_I^0 , ω_S^{NOM} , and the sweep range Δ , it can happen
337 that double-quantum conditions are fulfilled in some places within the sample when the values are
338 scaled by the RF field inhomogeneity. The double quantum conditions are governed by the formula

$$\begin{aligned}
\omega_I + \omega_S - n\omega_R &= \xi(z)[\omega_I^{NOM} + \omega_S^{NOM}] - n\omega_R \\
&= \xi(z)[\omega_I^0 + f(t) + \omega_S^{NOM}] - n\omega_R \quad (41) \\
&= \xi(z)f(t) + \xi(z)(\omega_I^0 + \omega_S^{NOM}) - n\omega_R
\end{aligned}$$

339 which is represented in red in Figure 4C. While the values ω_I^0 , ω_S^{NOM} are satisfying the zero quantum
340 $n = +1$ condition around the center of the coil, at the same time, they satisfy the double quantum
341 $n = +2$ condition towards the ends of the coil (places where the red area crosses zero value). As a
342 result, there are parts of the sample that produce positive magnetization transfer and parts that
343 experience negative transfer. Thus, the overall efficiency of the experiment is decreased.

344



345

346 **Figure 4:** Visualization of the RF sweep ranges as a function of the position of a particular spin packet
 347 along the coil axis. The Hartmann-Hahn resonance condition is artificially defined for a sweep
 348 frequency 0 kHz. (A) The sweep range (green area) is evaluated according to Eq. (39) for $n = +1$ and
 349 assuming an MAS frequency of 50 kHz. The blue arrows indicate the direction of the sweep for an RF
 350 inhomogeneity factor of $\xi=0.8$ and 1.0. The sweep amplitude Δ corresponds to 10 kHz and 30 kHz in
 351 (A) and (B), respectively. (C) Overlay of the RF amplitude sweeps evaluated for the ZQ ($n = +1$)
 352 matching condition (Eq. (39), green) and DQ ($n = +2$) matching condition (Eq. (41), red) with nominal
 353 RF amplitudes $\omega_I^{NOM}/2\pi=95$ kHz and $\omega_S^{NOM}/2\pi=45$ kHz. These values were selected to demonstrate
 354 that the ZQ matching condition is satisfied in the center of the coil, and simultaneously a DQ is
 355 encountered for spin packets in regions of the sample where the RF amplitudes are scaled down by
 356 the RF field inhomogeneity.

357

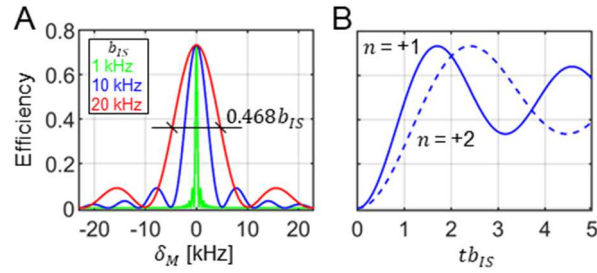
358 3. Results and Discussion

359 3.1. CP matching profile

360 Experimentally, optimal cross polarization conditions are found in experiments in which the RF
 361 amplitude on one of the RF channels is systematically varied to yield the highest sensitivity. In case the
 362 Hartmann-Hahn recoupling condition is very narrow, this can be difficult as many repetitions with a
 363 small increment of the RF amplitude are required. In the Theory section, we derived analytical formulas
 364 for the CP matching profiles for constant RF amplitudes. We have found that for a homogeneous RF
 365 field distribution, the width at half height of the recoupling condition is governed by the size of the
 366 dipolar coupling and can be estimated as $0.468b_{IS}$ after powder averaging. Both the width and the
 367 maximal transfer efficiency are independent of the MAS frequency. Maximum transfer of 73% is
 368 achieved for mixing times satisfying the condition $tb_{IS} = 1.7$ for the $n = \pm 1$ recoupling conditions.
 369 The same efficiency is obtained for the $n = \pm 2$ conditions. However, due to the different spatial
 370 dependence and scaling factors in g_1 and g_2 terms (Eqs. (3) and (4)) the maximum is achieved there

371 for mixing times $tb_{IS} = 2.4$. These facts are well known and are presented graphically in Figure 5.
 372 Figure 5A shows the CP matching profile calculated using Eq. (27) and (30) for $n = +1$ and assuming a
 373 dipolar coupling constant b_{IS} of 1, 10, and 20 kHz, which are the characteristic values for ^{13}C - ^{15}N , ^1H -
 374 ^{15}N , and ^1H - ^{13}C spin pairs, respectively. $\langle \epsilon^{ZQ,+1} \rangle_{\text{powder}}$ is represented as a function of the RF amplitude
 375 mismatch $\delta_M/2\pi = \omega_I - \omega_S - \omega_R$ with respect to the exact Hartmann-Hahn.

376



377

378 **Figure 5:** Properties of the constant amplitude CP experiment assuming homogeneous RF fields. (A)
 379 The width of the CP matching profile around the zero-quantum ($n=+1$) Hartmann-Hahn matching
 380 condition depends on the dipolar coupling strength b_{IS} . (B) Magnetization buildup of the transferred
 381 magnetization for the $n=+1$ and $n=+2$ matching condition. Independently of the MAS frequency and
 382 b_{IS} , the $n=+2$ condition reaches the same maximum, however, at longer mixing times. The curves were
 383 calculated using Eqs. (27) and (30).

384

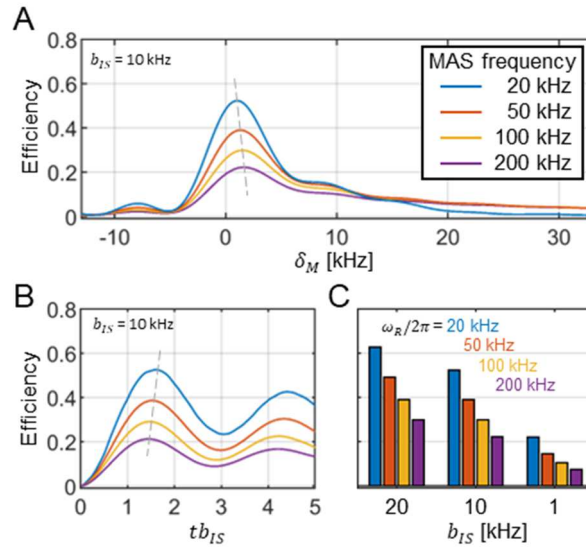
385 For inhomogeneous RF fields, the CP matching profile can be quantitatively described by inserting Eq.
 386 (31) into Eq. (27) and taking the average in Eq. (32). Figure 6A shows the influence of inhomogeneous
 387 RF fields and the induced asymmetric broadening of the matching profile $\langle \epsilon^{ZQ,+1} \rangle_{\text{powder}}^{rf-inh}$. Clearly, the
 388 maximal transfer efficiency substantially decreases with increasing MAS frequency.

389 A closer inspection of the CP matching profiles in Figure 6A reveals that the maximum overall transfer
 390 efficiency is not reached for the exact ZQ ($n = +1$) condition with $\omega_I^{NOM} - \omega_S^{NOM} = \omega_R$,
 391 corresponding to $\delta_M = 0$. In practice, it is advantageous to set ω_I^{NOM} little higher and thus shift the
 392 volume element where the Hartmann-Hahn condition is matched away from the center of the coil.
 393 This allows to partially compensate for the destructive effect of the RF field inhomogeneity. This
 394 mismatch δ_M of the Hartmann-Hahn matching condition is naturally found during the experimental
 395 setup when the RF fields are optimized to experimentally yield the best efficiency. However, the
 396 mismatch is small (a few kHz at most) and generally decreases with decreasing MAS frequency (see
 397 the dashed line in Figure 6A). Similarly, the RF field inhomogeneity has a subtle effect on the buildup
 398 of the transferred magnetization. Figure 6B shows that maximum transfer occurs at shorter mixing
 399 times for increased MAS frequencies.

400 Figure 6C shows how decreasing dipolar couplings result in a diminished Hartmann-Hahn transfer
 401 efficiency. The calculations are carried out for three typical dipolar coupling values, and for MAS
 402 frequencies in the range of 20 kHz to 200 kHz. Strikingly, for $\omega_R/2\pi = 200$ kHz and $b_{IS} = 1$ kHz, the
 403 maximum transfer is only about 7%.

404 We used numerical simulations in SIMPSON (Bak et al., 2000; Tosner et al., 2014) to verify the
 405 predictions of the analytical model. To implement an experiment, specific values of ω_I and ω_S need to
 406 be selected. Consideration of RF field inhomogeneity increases the complexity of this selection process,
 407 since certain values of ω_I , ω_S can lead to a situation in which ZQ and DQ recoupling conditions are
 408 fulfilled simultaneously in different parts of the sample (Figure 4C). This phenomenon was explored
 409 experimentally by Gupta et al. (Gupta et al., 2015). In case this situation is avoided, we find perfect
 410 agreement between the analytical model and the numerical simulations (data not shown).

411



412

413 **Figure 6:** Transfer efficiency of the constant amplitude CP experiment in the presence of RF field
 414 inhomogeneity and assuming a dipolar coupling strength $b_{IS} = 10$ kHz. For the calculation, a rotor fully
 415 packed with material is assumed. (A) The maximum of the CP matching profile decreases with
 416 increasing MAS frequency for the zero-quantum ($n=+1$) condition. At the same time, the width
 417 increases. A grey dashed line is used to indicate the position of the maximum. The maximum of the CP
 418 matching profile shifts to higher mismatch values δ_M for increased MAS frequencies. (B) Magnetization
 419 buildup curves for different MAS frequencies. The legend is indicated in panel (A). With increasing MAS
 420 frequencies, magnetization reaches the maximum transfer at shorter mixing times. (C) Maximum
 421 transfer efficiencies for the characteristic dipolar coupling values b_{IS} of 1, 10 and 20 kHz for different
 422 MAS frequencies. Data were generated using Eqs. (27), (31) and (32).

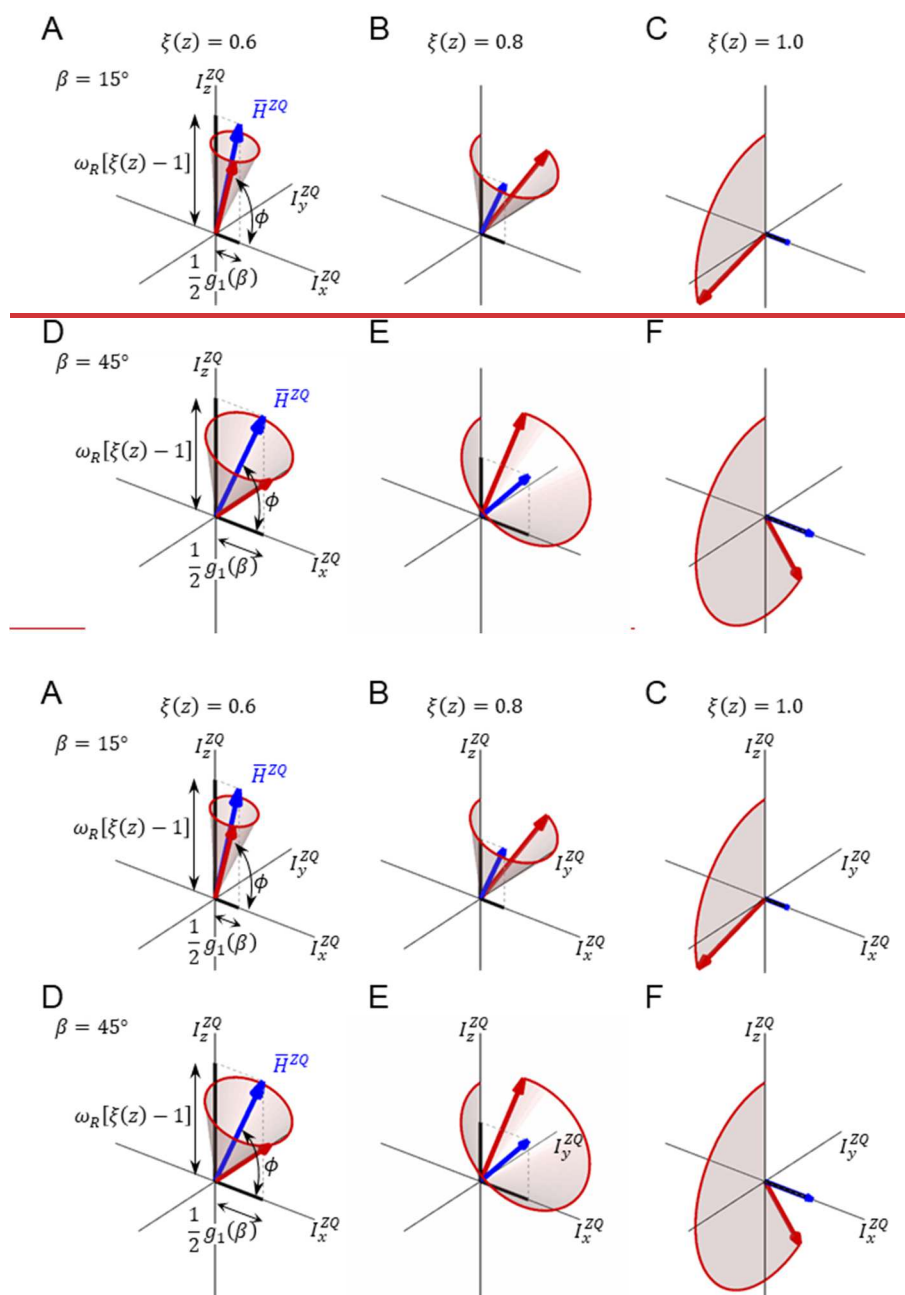
423

424 3.2. Visualization of the magnetization transfer trajectories

425 In the following, we aim to visualize the spin trajectory during the CP experiment in its basic form with
 426 constant RF and with RF amplitude sweeps. We focus on the vicinity of the ZQ ($n = +1$) Hartmann-
 427 Hahn condition and use the effective Hamiltonian \bar{H}^{ZQ} given in Eq. (34) for the analysis. We consider
 428 RF field inhomogeneity and assume nominal RF amplitudes that match the recoupling condition in the
 429 center of the coil, $\omega_I^{NOM} - \omega_S^{NOM} = \omega_R$. Figure 7 shows the spin dynamics for two crystallite
 430 orientations ($\beta=15^\circ$ and 45°), and three positions within the coil ($\xi=0.6, 0.8, \text{ and } 1.0$). These conditions
 431 are highlighted in Figure 1 and Figure 2. In the center of the coil where $\xi=1.0$, the Hamiltonian \bar{H}^{ZQ}

432 (blue vector) is aligned with the I_x^{ZQ} axis. The spin state vector $\rho^{ZQ}(t)$ (red vector) rotates in circles
 433 within the yz plane with an angular velocity that depends on the crystallite orientation (Figure 7C,F).
 434 This situation corresponds to the case without RF field inhomogeneity.

435 Depending on the position within the coil, a mismatch contribution in the effective Hamiltonian \bar{H}^{ZQ}
 436 along the I_z^{ZQ} axis is obtained, which is according to Eq. (34) proportional to the MAS frequency. The
 437 effective rotation axis is tilted away from the I_x^{ZQ} direction by an angle ϕ , Eq. (23). The effective
 438 rotation frequency $\omega_{eff}^{ZQ,+1}$, Eq. (22), increases with increasing mismatch. Likewise, the I_x^{ZQ} component
 439 of \bar{H}^{ZQ} decreases with the decreasing effective dipolar coupling. This amplifies the effect of the RF
 440 field inhomogeneity on the orientation of the effective Hamiltonian axis. The state vector rotates on
 441 the surface of a cone (Figure 7AB,DE). As a consequence, the inversion becomes inefficient. Only the
 442 central part of the sample yields a high transfer efficiency.



443

444

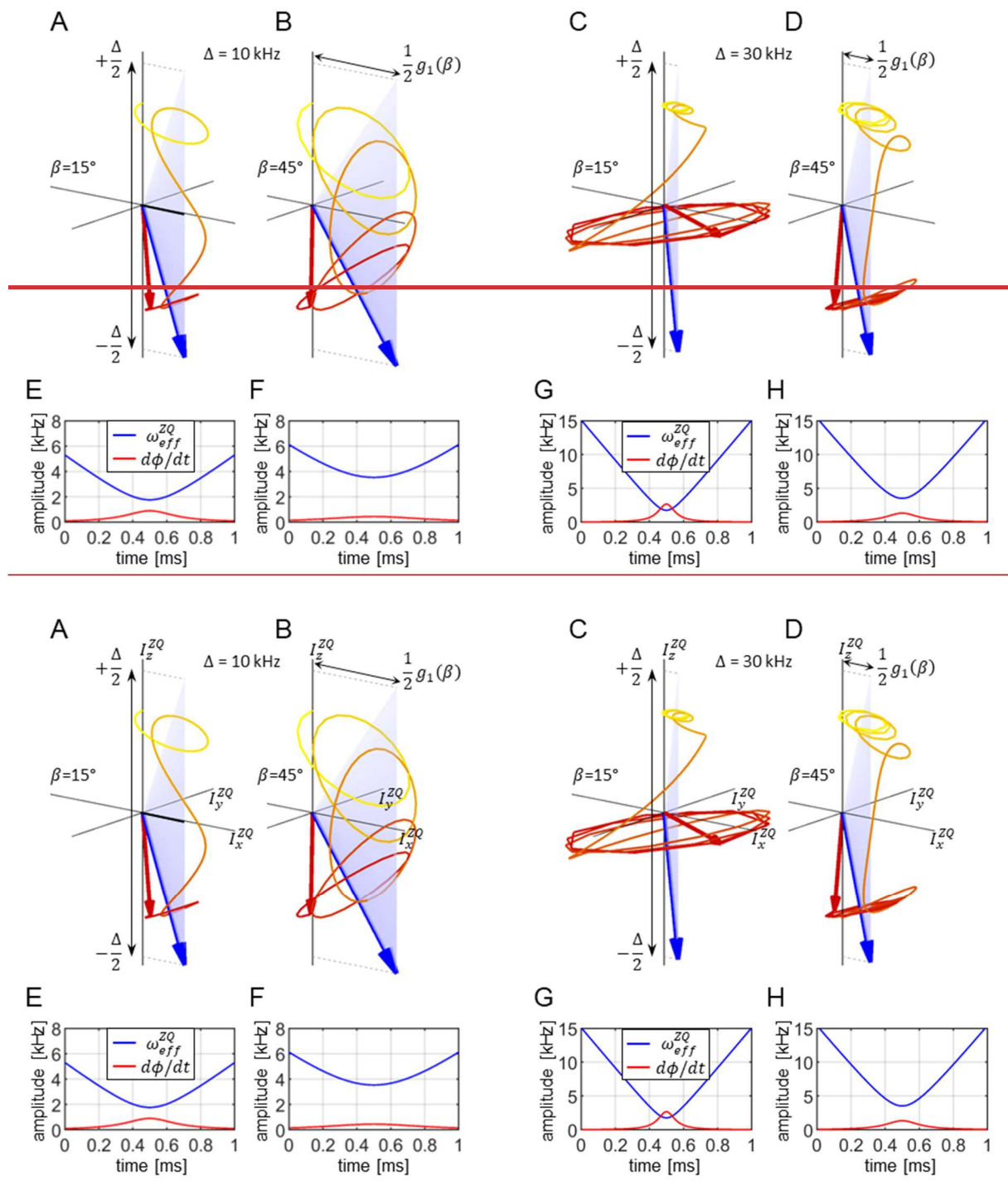
445 **Figure 7.** Visualization of the spin state trajectories for the constant amplitude cross-polarization
 446 experiment evaluated for two crystal orientations. (A-C) crystallite orientation $\beta=15^\circ$, (D-F) $\beta=45^\circ$. The
 447 calculations were carried out for 3 positions along the coil axis that correspond to RF field scaling values
 448 of $\xi(z)=0.6$ (panels A/D), 0.8 (panels B/E), and 1.0 (panels C/F). The state vector, ρ^{ZQ} , is represented
 449 by a red vector. The effective Hamiltonians are represented by blue vectors. ρ^{ZQ} rotates around \bar{H}^{ZQ}
 450 on the surface of a cone (shaded area). In the simulation, an MAS frequency of 50 kHz and $b_{IS}=10$ kHz
 451 was assumed.

452

453 **3.3. RF amplitude sweeps in the absence of RF field inhomogeneity**

454 Continuous RF amplitude sweeps are used to improve the cross polarization efficiency. In this case, the
 455 effective Hamiltonian changes its orientation in the course of the pulse sequence. An adiabatic
 456 inversion is achieved if two conditions are fulfilled: (i) the initial state vector is aligned with the initial
 457 effective field vector and (ii) the effective field changes its orientation slowly. We focus on the zero
 458 quantum ($n = +1$) condition assuming a dipolar coupling constant $b_{IS}= 10$ kHz. In the following, spin
 459 state trajectories are calculated for two sweep amplitudes, $\Delta = 10$ kHz and 30 kHz.

460 The spin state trajectories for the linear ramp are represented in Figure 8. The I_x^{ZQ} component of the
 461 effective Hamiltonian is fixed in time, and is given by the effective dipolar coupling at a given
 462 orientation (Eq. (40), assuming $\xi=1.0$). The maximal value of $\frac{1}{2}g_1(\beta)$ is reached for $\beta=45^\circ$ which
 463 together with the sweep amplitude of $\Delta=10$ kHz and according to Eq. (23) results in a tilt angle of the
 464 effective field $\phi(t = 0, \beta = 45^\circ)=54.7^\circ$ at the beginning of the pulse sequence (Figure 8B). Clearly, the
 465 initial state vector $\rho^{ZQ}(0) = I_z^{ZQ}$ is not aligned with the effective field of $\bar{H}^{ZQ}(t = 0)$. However, the
 466 inversion efficiency is high due to the slow change of the orientation of the effective field, $d\phi/dt$, such
 467 that the state vector can follow the effective field while it is rotating around it in rather large circles
 468 (see evaluation of the adiabaticity condition in Figure 8F). For a smaller effective dipolar coupling (for
 469 example, $\beta=15^\circ$ in Figure 8A), the angle ϕ is larger, close to 90° . During the linear ramp, the effective
 470 Hamiltonian amplitude $\omega_{eff}^{ZQ}(t)$ goes through a minimum in the middle of the sweep at $t = T/2$, where
 471 its value is solely determined by the effective dipolar coupling, see Eq. (22). At the same time, $d\phi/dt$
 472 reaches its maximum (Figure 8E). Under these conditions, the state vector keeps track with the
 473 effective field (Figure 8A). When a larger sweep amplitude is employed, e.g. $\Delta=30$ kHz, the orientation
 474 of the initial effective field is closer to the I_z^{ZQ} axis, $\phi(t = 0, \beta = 45^\circ)=76.7^\circ$ (Figure 8D). At the same
 475 time, the amplitude of the effective Hamiltonian $\omega_{eff}^{ZQ}(t = 0)$ is increased as well. For the crystallite
 476 orientation $\beta=15^\circ$ (Figure 8C), however, we find that the adiabaticity condition is violated in the middle
 477 of the pulse sequence (Figure 8G). The state vector is not able to follow the effective field as $d\phi/dt$
 478 becomes too high. As a consequence, the state vector keeps rotating near the equator (Figure 8C) and
 479 thus contributes little to the total transfer efficiency.



480

481

482 **Figure 8.** Visualization of the spin state trajectories for the linear ramp cross-polarization experiment
 483 assuming a homogeneous RF field distribution. For the simulation, a dipolar coupling $b_{IS}=10$ kHz was
 484 assumed. The CP contact time was set to $T=1$ ms. The calculation was carried out for two crystallite
 485 orientations ($\beta=15^\circ$ and 45° , panels A,C and B,D, respectively), and two sweep amplitudes ($\Delta=10$ kHz
 486 and $\Delta=30$ kHz, panels A,B and C,D, respectively). The blue-shaded areas represent the changing
 487 effective Hamiltonian. The blue arrow indicates the effective Hamiltonian at the end of the pulse
 488 sequence at $t = T$. The component along the I_z^{ZQ} -axis is time dependent, while the I_x^{ZQ} -axis
 489 component is fixed (see Eq. (40)). The beginning of the trajectory is depicted as a yellow line which
 490 gradually turns into red as the trajectory progresses. The final state of the spin state vector (initially

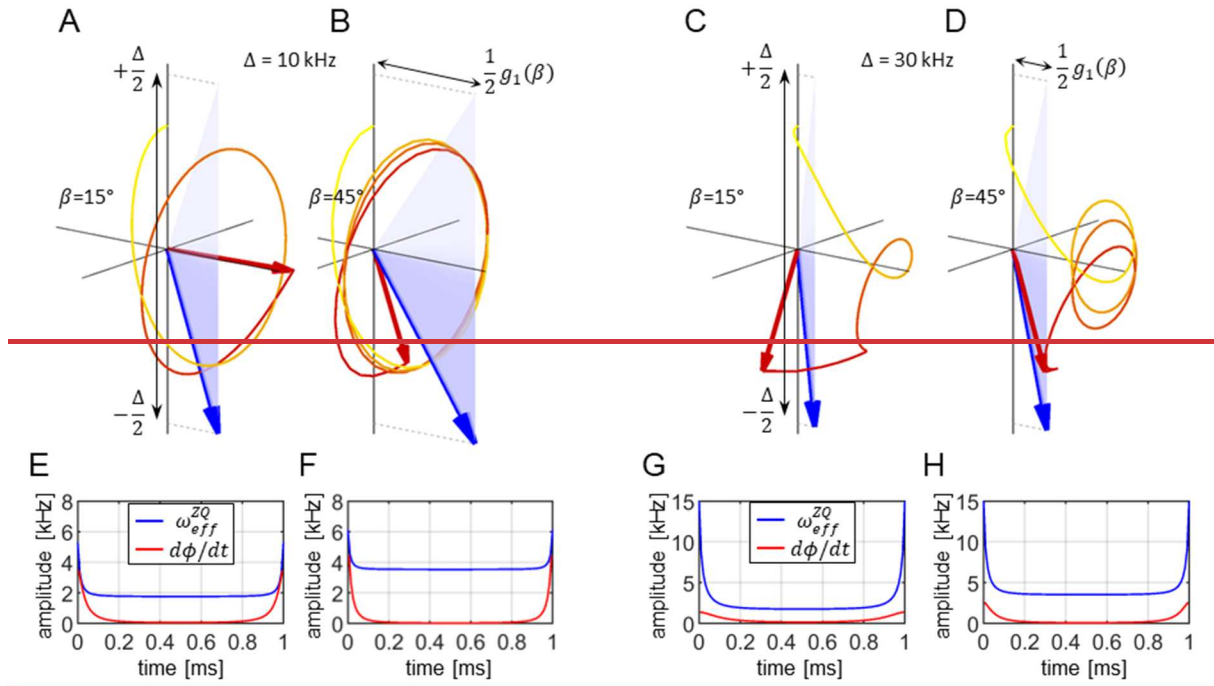
491 oriented along I_z^{ZQ}) is drawn as a red arrow. Panels E-H display $d\phi(t)/dt$ and $\omega_{eff}^{ZQ}(t)$. In C/G, the
492 adiabaticity condition $d\phi/dt < \omega_{eff}$ is violated during the sweep.

493

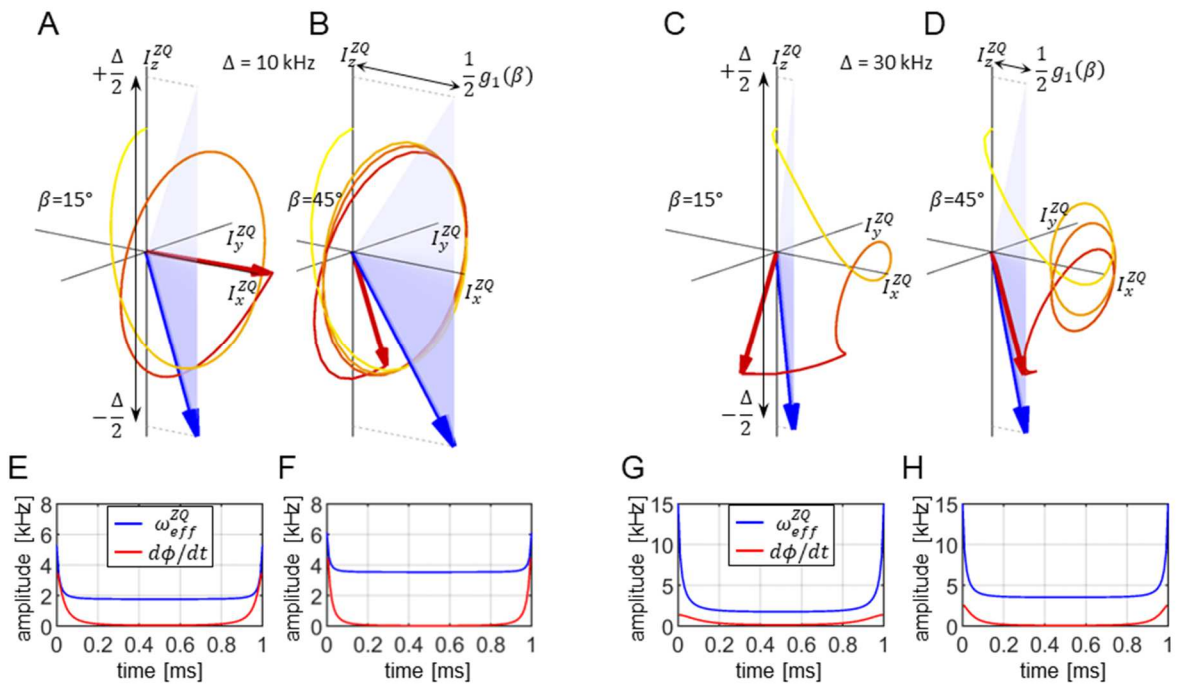
494 Spin state trajectories for the adiabatic variant of the CP experiment are shown in Figure 9. The
495 tangential sweep has been suggested to keep the rate of change $d\phi(t)/dt$ small compared to the
496 effective field amplitude at all times (Hediger et al., 1995). Initially, $\omega_{eff}(t)$ is large implicating that
497 $d\phi(t)/dt$ can be large. However, for small sweep amplitudes such as $\Delta=10$ kHz the effective field
498 changes too rapidly for a portion of crystallites at the beginning and at the end of the sweep so that
499 the adiabaticity condition is violated (Figure 9E). Most of the dynamics takes place when the tangential
500 function goes through the central plateau, where the RF amplitudes do not change significantly over
501 an extended period of time. The state vector rotates in large circles around the effective Hamiltonian
502 that is oriented predominantly along the I_x^{ZQ} axis. When a larger sweep amplitude $\Delta = 30$ kHz is used,
503 the adiabatic regime is restored for most crystallite orientations and an improved transfer efficiency is
504 obtained.

505 Figure 10 compares the magnetization transfer during the RF sweep for the examples discussed above.
506 The transfer process is fast when the change of the effective field orientation is fast: in the middle of
507 the linear ramp, and at the beginning and at the end of the tangential sweep, provided the adiabaticity
508 condition is maintained (Figure 10AB). Figure 10CD shows the transfer efficiency as a function of
509 crystallite orientation. Note that the spin state inversion cannot be achieved for crystallite orientations
510 with an effective dipolar coupling that is vanishing, i.e., for $\beta=0^\circ$ and 90° . The portion of crystallites
511 yielding low transfer depends on the ratio of the sweep amplitude Δ and the dipolar coupling b_{IS} . For
512 the linear ramp $\Delta=10$ kHz is preferable, while the tangential sweep using an amplitude $\Delta = 30$ kHz yields
513 high efficiency for most of the crystallites under the conditions investigated here. After powder
514 averaging, the magnetization transfer efficiency is on the order of 90% for the tangential sweep. We
515 would like to note that all predictions based on the ZQ average Hamiltonian agree well with exact
516 simulations using SIMPSON (data not shown).

517



518

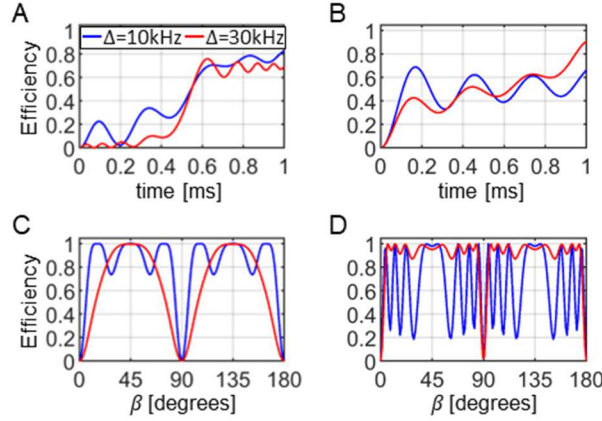


519

520 **Figure 9:** Visualization of the spin state trajectories for the adiabatic tangential sweep cross-
 521 polarized experiment assuming a homogeneous RF field distribution. For the simulation, a dipolar
 522 coupling $b_{IS}=10$ kHz was assumed. The CP contact time was set to $T=1$ ms. The calculation was carried
 523 out for two crystallite orientations ($\beta=15^\circ$ and 45° , panels A,C and B,D, respectively) and two sweep
 524 amplitudes ($\Delta=10$ kHz and $\Delta=30$ kHz, panels A,B and C,D, respectively, $b = \Delta/50$). The blue-shaded
 525 areas represent the changing effective Hamiltonian. The blue arrow indicates the effective Hamiltonian
 526 at the end of the pulse sequence at $t = T$. The component along the I_z^{ZQ} -axis is time dependent, while
 527 the I_x^{ZQ} -axis component is fixed (see Eq. (40)). The beginning of the trajectory is depicted as a yellow
 528 line which gradually turns into red as the trajectory progresses. The final state of the spin state vector

529 (initially oriented along I_z^{ZQ}) is drawn as a red arrow. Panels E-H display $d\phi(t)/dt$ and $\omega_{eff}^{ZQ}(t)$. In A/E
 530 and B/F, the adiabaticity condition $d\phi/dt < \omega_{eff}$ is violated during the sweep.

531



532

533 **Figure 10:** Powder averaged buildup of the transferred magnetization during the mixing time of the CP
 534 experiment (A, B) and the final transfer efficiency as a function of crystallite orientation (C, D) for an
 535 RF amplitude sweep using a linear ramp (A,C) and a tangential shape (B, D). The blue and red curves
 536 correspond to sweep amplitudes of 10 and 30 kHz, respectively. In all simulations, a homogeneous RF
 537 field distribution is assumed.

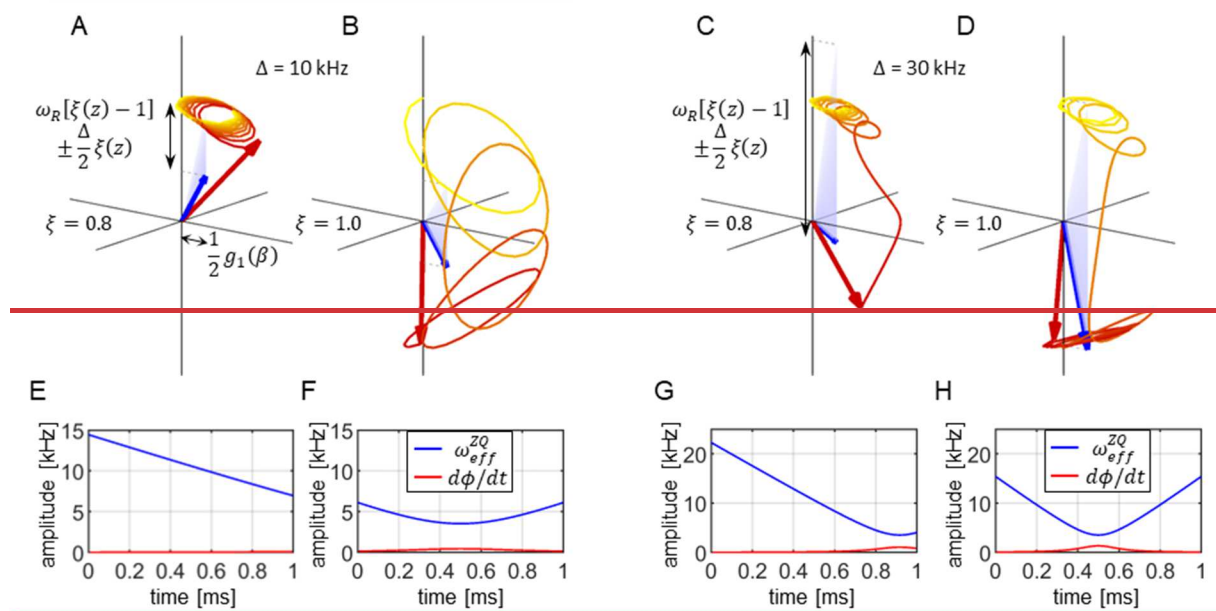
538

539 **3.4. RF amplitude sweeps in the presence of an inhomogeneous RF field**

540 In the following paragraph, RF field inhomogeneities are included in the analysis. For simplicity, we
 541 assume that the RF field varies along the solenoid coil axis as described in Figure 2 and the variation is
 542 the same for both RF channels. We disregard time modulations induced by sample rotation in a
 543 spatially inhomogeneous RF field. We assume that the Hartmann-Hahn condition is fulfilled for the
 544 nominal RF amplitudes in the middle of the coil. The RF amplitude sweep is applied to the I channel.
 545 We again examine the zero-quantum ($n = +1$) recoupling condition. The drive Hamiltonian \bar{H}^{ZQ} is
 546 given by Eq. (40). Sweeping the RF amplitude makes the I_z^{ZQ} -component of the effective Hamiltonian
 547 time dependent. The range over which it varies depends on the position along the coil axis, and it is
 548 visualized in Figure 4. The center of the sweep is shifted away from the exact matching condition
 549 towards the ends of the coil by an amount that depends on the MAS frequency. As discussed above,
 550 the evolution in the double-quantum subspace can be neglected, since \bar{H}^{DQ} has a dominant
 551 component along I_z^{DQ} axis which is much larger than the effective dipolar coupling. This can be
 552 achieved by choosing a proper value for ω_S^{NOM} . At the same time, we have chosen conditions that
 553 avoid simultaneous matching of different Hartmann-Hahn conditions within the sample volume.

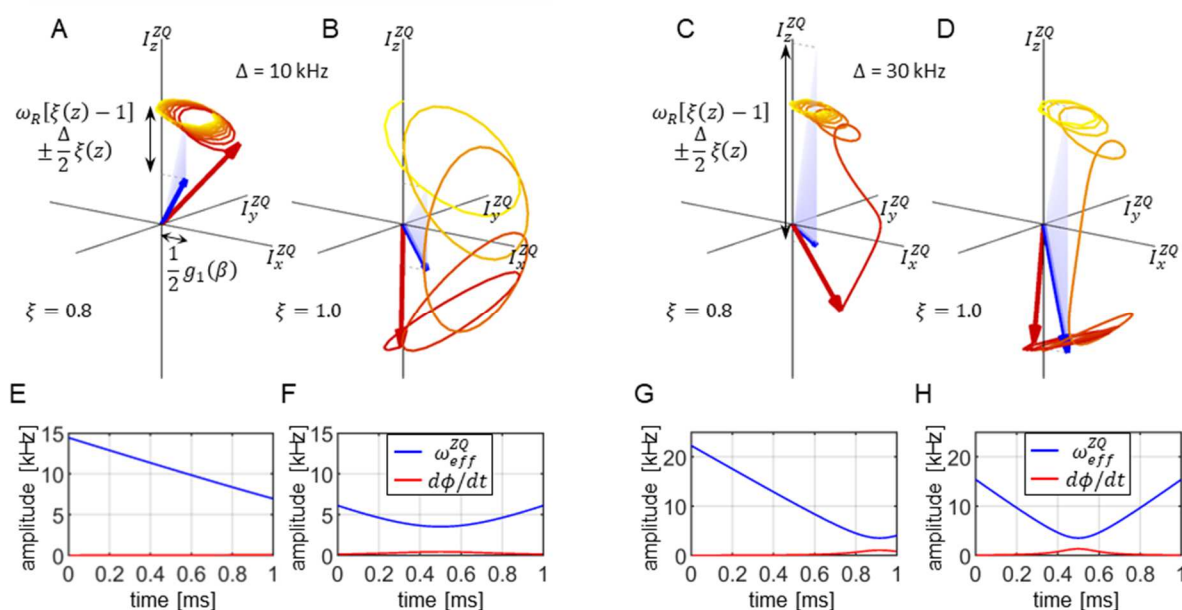
554 The previous description of the RF amplitude modulated CP is valid in the center of the coil where
 555 $\xi=1.0$. The situation is quite different in volume elements towards the ends of the coil. Figure 11
 556 illustrates the spin state trajectories for the linear ramp CP experiment, assuming a crystallite angle
 557 $\beta=45^\circ$, a MAS frequency of $\omega_R/2\pi=50$ kHz, and a dipolar coupling constant of $b_{IS}=10$ kHz. The scaling
 558 factor $\xi=0.8$ is realized for $z = \pm 0.36l$ (where l is the coil length) around the center of the coil. When

559 the sweep amplitude is $\Delta=10$ kHz, the effective field does not get inverted during the sweep (Figure 4A
 560 and Figure 11A) and therefore cannot invert the spin state, regardless of its adiabaticity (Figure 11E).
 561 Increasing the sweep amplitude to $\Delta=30$ kHz yields better results as the effective field approaches the
 562 Hartmann-Hahn recoupling condition towards the end of the sweep period (Figure 4B and Figure 11C).



563

564



565

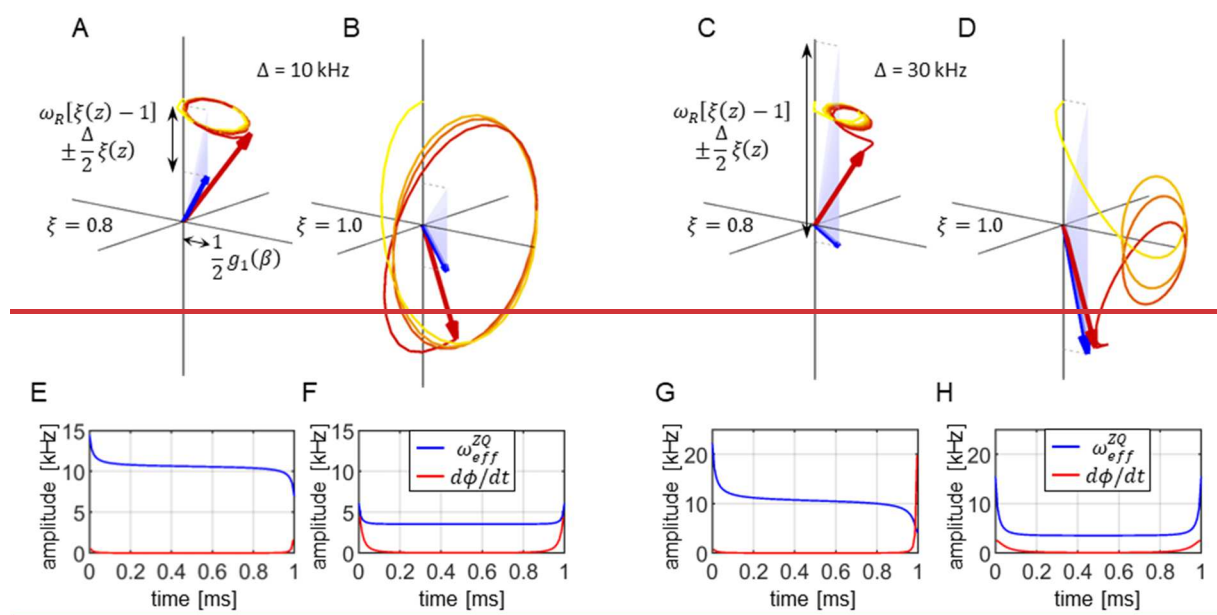
566 **Figure 11:** Visualization of the spin state trajectory for a linear ramp cross-polarization experiment
 567 assuming an inhomogeneous RF field distribution. For the simulation, a dipolar coupling $b_{IS}=10$ kHz
 568 was assumed. The CP contact time was set to $T=1$ ms. The calculation was carried out for one crystallite
 569 orientation ($\beta=45^\circ$) and two positions along the coil axis with RF field scaling factors $\xi=0.8$ and 1.0
 570 (panels A,C and B,D) and two sweep amplitudes $\Delta=10$ kHz and $\Delta=30$ kHz (panels A,B and C,D). The blue-
 571 shaded areas represent the changing effective Hamiltonian. The blue arrow indicates the effective

572 Hamiltonian at the end of the pulse sequence at $t = T$. The component along the I_z^{ZQ} -axis is time
 573 dependent, while the I_x^{ZQ} -axis component is fixed (see Eq. (40)). The beginning of the trajectory is
 574 depicted as a yellow line which gradually turns into red as the trajectory progresses. The final state of
 575 the spin state vector (initially oriented along I_z^{ZQ}) is drawn as a red arrow. Panels E-H display $d\phi(t)/dt$
 576 and $\omega_{eff}^{ZQ}(t)$ to appreciate whether the adiabaticity condition $d\phi/dt < \omega_{eff}$ is violated during the
 577 sweep.

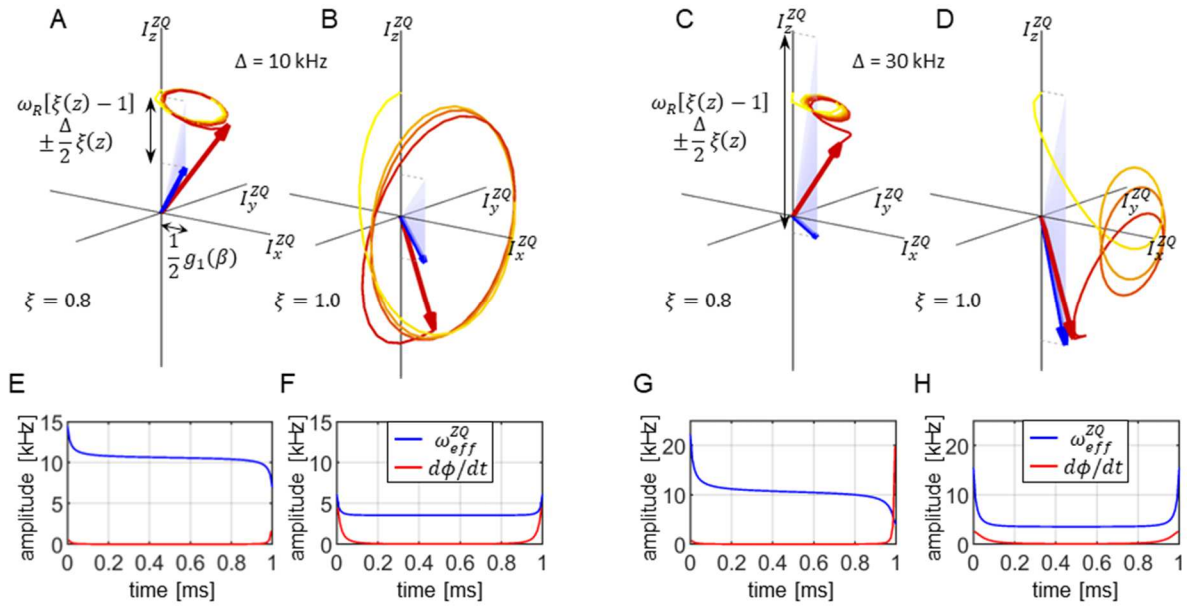
578

579 For a tangential sweep, the spin state trajectories are depicted in Figure 12. Initially, and towards the
 580 end of the sweeping period, the RF amplitude changes rapidly and so does the effective field
 581 orientation. This can lead to a violation of the adiabaticity condition, as encountered for the calculation
 582 with a sweep amplitude of $\Delta=30$ kHz (Figure 12C,G). Despite the fact that the Hartmann-Hahn matching
 583 condition is included within the sweep range, the state vector does not follow the effective field. These
 584 parts of the sample yield a low transfer efficiency.

585



586



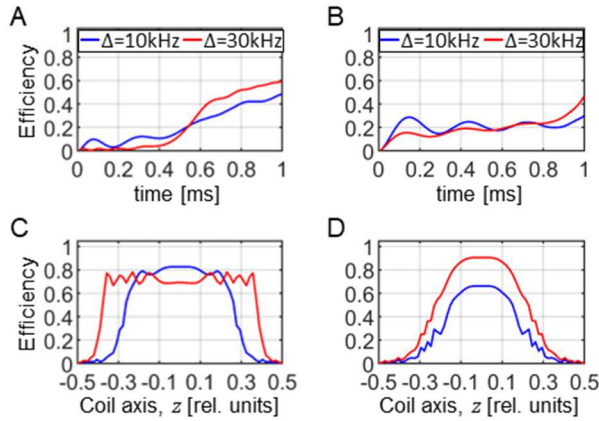
587

588 **Figure 12:** Visualization of the spin state trajectory for an adiabatic tangential sweep cross-polarization
 589 experiment assuming an inhomogeneous RF field. For the simulation, a dipolar coupling $b_{IS}=10$ kHz
 590 was assumed. The CP contact time was set to $T=1$ ms. The calculation was carried out for one crystallite
 591 orientation ($\beta=45^\circ$) and two positions along the coil axis with RF field scaling factors $\xi=0.8$ and 1.0
 592 (panels A,C and B,D) and two sweep amplitudes $\Delta=10$ kHz and $\Delta=30$ kHz, assuming $b = \Delta/50$ (panels
 593 A,B and C,D). The blue-shaded areas represent the changing effective Hamiltonian. The blue arrow
 594 indicates the effective Hamiltonian at the end of the pulse sequence at $t = T$. The component along
 595 the I_z^{ZQ} -axis is time dependent, while the I_x^{ZQ} -axis component is fixed (see Eq. (40)). The beginning of
 596 the trajectory is depicted as a yellow line which gradually turns into red as the trajectory progresses.
 597 The final state of the spin state vector (initially oriented along I_z^{ZQ}) is drawn as a red arrow. Panels E-
 598 H display $d\phi(t)/dt$ and $\omega_{eff}^{ZQ}(t)$ to appreciate whether the adiabaticity condition $d\phi/dt < \omega_{eff}$ is
 599 violated during the sweep.

600

601 The buildup of the transferred magnetization integrated over the sample volume and detected by the
 602 NMR coil for both the linear ramp and the tangential sweep is presented in Figure 13A,B. It is not
 603 obvious which sweeping method will yield a higher total transfer efficiency. Of the four setups
 604 discussed so far, the linear ramp with $\Delta=30$ kHz yields the best result. When comparing efficiency
 605 profiles along the coil axis (Figure 13C,D) we observe that tangential sweep is more efficient near the
 606 center of the coil but quickly loses efficiency when going towards the ends. However, linear ramp yields
 607 equal transfer over a larger sample volume.

608



609

610 **Figure 13:** Powder averaged buildup of transferred magnetization during the mixing time of the CP
 611 experiment (A, B), and the final powder averaged transfer efficiency as a function of the position along
 612 the coil axis (C, D) for a linear ramp (A,C) and a tangential shape (B, D). The blue and red curves
 613 correspond to sweep amplitudes of $\Delta=10$ kHz and $\Delta=30$ kHz, respectively. In the calculation, an
 614 inhomogeneous RF field is assumed.

615

616 **3.5. Numerical optimizations of linear and tangential sweeps**

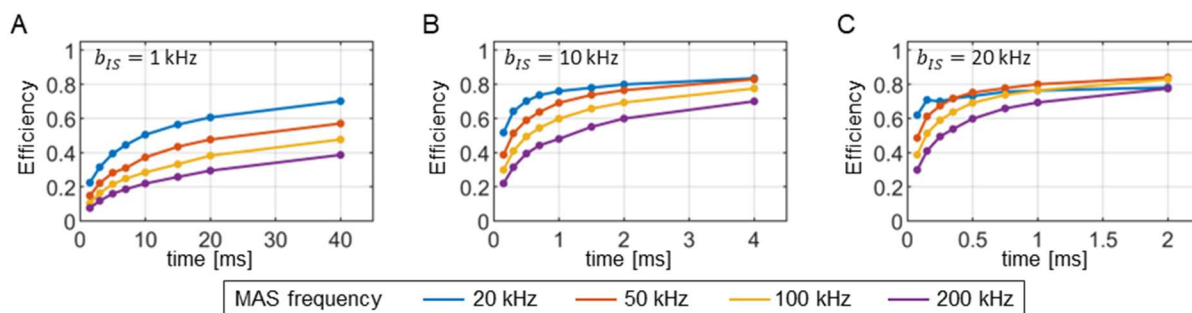
617 In this section, we discuss which parameters of a linear ramp and a tangential sweep yield the best
 618 transfer efficiency. We address this problem by a numerical optimization. The calculations are
 619 repeated for a range of dipolar couplings and MAS frequencies. In the case of the linear ramp, the
 620 sweep amplitude Δ and the offset δ_M from the exact Hartmann-Hahn condition are optimized. In case
 621 of the tangential sweep, the curvature parameter b is considered in addition (Figure 3). The offset
 622 parameter δ_M corresponds to the mismatch of the recoupling condition in the middle of the coil due
 623 to RF inhomogeneity and reflects the experimental optimization procedure where the amplitude
 624 ω_S^{NOM} is kept constant and the amplitude ω_I^0 is optimized around the expected recoupling condition.
 625 To ensure that not more than one matching condition is encountered during the sweep, the amplitude
 626 Δ was restricted to values within $\pm\omega_R/2$ (Hediger et al., 1995). The dynamics was evaluated using the
 627 effective Hamiltonian \bar{H}^{ZQ} given in Eq. (40). The optimized parameters correspond to the best transfer
 628 efficiency obtained from 100 repetitions initiated by random guess. As expected, we obtain a different
 629 set of optimal parameters for each contact time, dipolar coupling, and MAS frequency.

630 The optimized transfer efficiencies are summarized in Figure 14. Remarkably, we have not found any
 631 significant differences in the performance of the linear ramp with respect to the tangential sweep.
 632 Both sweep methods yield the same total transfer efficiency, although they use different sweep
 633 parameters. An example of the best sweep shapes obtained for a dipolar coupling $b_{IS}=10$ kHz and an
 634 MAS frequency of 50 kHz is presented in Figure 15. The tangential sweeps tend to have a larger sweep
 635 amplitude Δ and a smaller offset values δ_M when compared to the linear ramp.

636 We observe that very long contact times are required to obtain high transfer efficiencies. For
 637 calculations involving different dipolar coupling strengths b_{IS} the same range of the reduced time
 638 parameter Tb_{IS} is used. In this way, longer mixing times T are maintained for smaller dipolar couplings
 639 b_{IS} . Better performance is obtained for cases with higher dipolar couplings which correlates with the

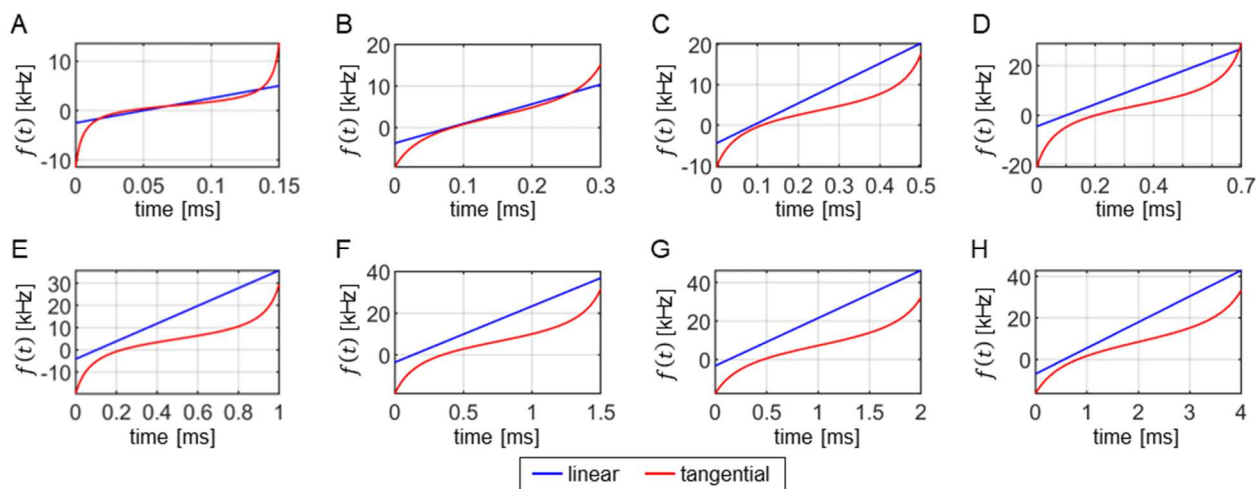
640 width of Hartmann-Hahn conditions in CP matching profiles. On the other hand, the transfer efficiency
 641 decreases at higher MAS frequencies due to increased volume selectivity. The most challenging are
 642 small dipolar couplings, on the order of 1 kHz and ultrafast MAS (>100 kHz) which are typical for ^{15}N -
 643 ^{13}C spin pairs in proteins studied by proton-detected MAS solid-state NMR experiments. To more
 644 efficiently average proton dipolar interaction, MAS probe development aims at smaller diameter
 645 rotors to achieve higher MAS rotation frequencies. Currently, 0.4 mm MAS probes are in development
 646 that can reach MAS frequencies of up to 200 kHz. Our predictions suggest that only 20% of the sample
 647 will contribute to the detected NMR signal after a 10 ms ^{15}N - ^{13}C CP mixing step at a MAS frequency of
 648 200 kHz, i.e. up to 80% of the signal is lost in a single magnetization transfer step. The efficiency
 649 increases to ca. 40% when a 40 ms long mixing period is used, provided that there are no signal losses
 650 due to relaxation. However, note that the sensitivity in a pulse sequence with multiple CP transfer
 651 elements depends on all previous transfer steps. The first CP element pre-selects a volume that is
 652 maintained or further restricted in subsequent transfer elements.

653



654

655 **Figure 14.** Maximum achievable transfer efficiencies in the cross-polarization experiment as a function
 656 of contact time and MAS frequency using numerical optimizations. Similar efficiencies are obtained for
 657 both the linear ramp and the tangential sweep, although different shape parameters have to be
 658 employed. Dipolar couplings of 1 kHz, 10 kHz and 20 kHz are used in the simulations for panels A, B,
 659 and C, respectively.



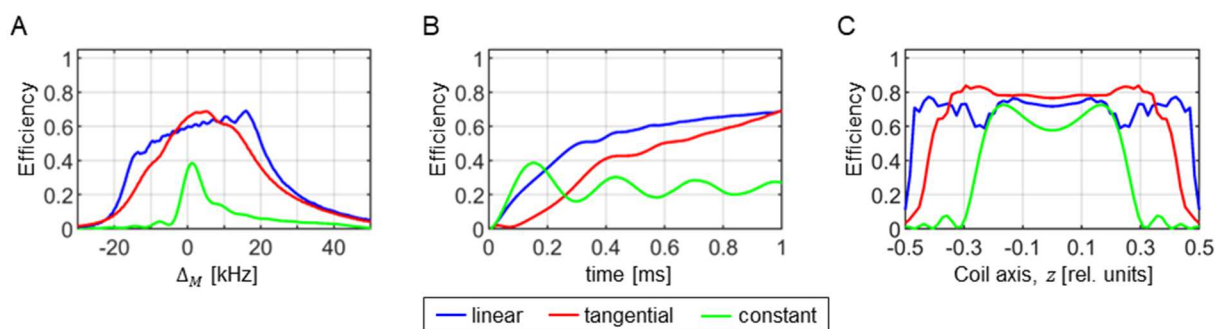
660

661 **Figure 15:** Comparison of optimal linear ramp (blue) and tangential sweep (red) shapes obtained by
 662 numerical optimizations at different contact times $T=0.15, 0.3, 0.5, 0.7, 1.0, 1.5, 2.0,$ and 4.0 ms in

663 panels A-H, respectively. For the optimization, a dipolar coupling $b_{IS}=10$ kHz was assumed. The
 664 calculations were performed assuming a MAS frequency of 50 kHz and a realistic RF inhomogeneity
 665 distribution. Although the two shapes are different, they yield virtually identical total transfer
 666 efficiencies.

667

668 We find that there is no difference between the linear ramp and the tangential shapes in terms of total
 669 transfer efficiency. In Figure 16, we compare these two methods (together with a constant amplitude
 670 CP) with respect to the width of the CP matching profile (panel A), the magnetization transfer buildup
 671 (panel B), and the sample volume selectivity (panel C). As expected, the RF amplitude sweep
 672 significantly improves the width and the height of the matching profile. The most important difference
 673 is that the tangential sweep yields higher efficiency near the center of the coil and lower efficiency at
 674 edges of the coil. Use of RF pulses and other recoupling elements can potentially result in a
 675 preselection of a particular sample volume that cannot be utilized by the linear ramp for a further
 676 transfer. Therefore, transfer elements should be optimized within the framework of the whole pulse
 677 sequence to minimize a differential preselection of the sample volume during calibration experiments.



678

679 **Figure 16:** Comparison of the matching profiles (A), magnetization transfer buildups (B), and
 680 contribution to the transfer efficiency of individual volume elements along the coil axis (C) for an
 681 optimized linear ramp (blue), a tangential sweep (red), and a constant amplitude CP (green). For the
 682 optimization, a dipolar coupling $b_{IS}=10$ kHz was assumed. The calculations were performed assuming
 683 a MAS frequency of 50 kHz and a realistic RF inhomogeneity distribution. The CP contact time was set
 684 to $T=1$ ms. In (A) and (C), the constant amplitude CP was evaluated after $160 \mu s$ when it reaches
 685 maximum transfer efficiency.

686

687 The linear ramp and the adiabatic tangential sweeps were calculated for the ZQ ($n = +1$) condition.
 688 However, the shapes are equally applicable to any other $n = \pm 1$ Hartmann-Hahn condition, as the
 689 corresponding effective Hamiltonian has the same form. The $n = \pm 2$ Hartmann-Hahn conditions
 690 suffer from increased RF field inhomogeneity (factor of 2 in Eq. 40) and have different powder
 691 averaging properties implied by the $g_2(\beta)$ term. Thus, a decreased CP transfer efficiency for the $n =$
 692 ± 2 matching condition is expected.

693

694 The transfer efficiencies of all pulse sequences were verified using numerical simulations in SIMPSON.
695 To avoid overlap of the different Hartmann-Hahn matching conditions, the zero quantum ($n = +1$)
696 condition with $\omega_S^{NOM}/2\pi = 60$ kHz was selected using MAS frequencies of 20 and 50 kHz, while the
697 double quantum ($n = +1$) condition with $\omega_S/2\pi = 30$ kHz was used for a MAS frequency of 100 kHz.
698 The agreement between SIMPSON and the effective Hamiltonian calculations is excellent except for a
699 simulation in which a dipolar coupling of 20 kHz and a MAS frequency of 20 kHz was assumed. In this
700 case, the numerically evaluated transfer efficiencies are about 10% lower. A plausible explanation is
701 that the first order average Hamiltonian approximation does not provide the full description of the
702 spin dynamics when the dipolar coupling and the MAS frequency are of similar value (in other cases it
703 holds $b_{IS} \ll \omega_R/2\pi$).

704

705 4. Conclusions

706 We have analyzed the magnetization transfer efficiency of the CP experiment as a function of the MAS
707 frequency in the presence of RF field inhomogeneity of a solenoid coil. We show that a sweep of the
708 RF amplitude through the Hartmann-Hahn matching conditions using either a linear ramp or a
709 tangential shape improves the performance in comparable way. We do not observe a difference in the
710 total transfer efficiency between these two methods. We find that magnetization transfer using a CP
711 recoupling element becomes inefficient in particular for small dipolar couplings for ultrafast MAS
712 experiments with rotation frequencies above 100 kHz. New recoupling methods that are designed
713 explicitly to account for inhomogeneous RF fields and ultrafast MAS conditions are needed to
714 overcome this issue in the future.

715

716 Author contribution

717 ZT and BR conceived the project. AŠ carried out numerical calculations. JB, AŠ, BR and ZT discussed the
718 results, sketched the plot of the paper, and collaborated on the final text. ZT wrote the paper.

719 Competing interests

720 At least one of the (co-)authors is a member of the editorial board of Magnetic Resonance.

721 Acknowledgements

722 Financial support was provided by the joint project between the Czech Science Foundation (20-00166J,
723 ZT) and Deutsche Forschungsgemeinschaft (Re 1435/20-1, BR).

724

725 References

726 Aebischer, K., Tošner, Z., and Ernst, M.: Effects of radial radio-frequency field inhomogeneity on MAS
727 solid-state NMR experiments, *Magnetic Resonance*, 2, 523–543, [https://doi.org/10.5194/mr-2-523-](https://doi.org/10.5194/mr-2-523-2021)
728 2021, 2021.

729 ANDREW, E. R., BRADBURY, A., and EADES, R. G.: Nuclear Magnetic Resonance Spectra from a Crystal
730 rotated at High Speed, *Nature*, 182, 1659–1659, <https://doi.org/10.1038/1821659a0>, 1958.

731 Bak, M., Rasmussen, J. T., and Nielsen, N. C.: SIMPSON: A general simulation program for solid-state
732 NMR spectroscopy, *J Magn Reson*, 147, 296–330, <https://doi.org/10.1006/jmre.2000.2179>, 2000.

733 Baum, J., Tycko, R., and Pines, A.: Broadband and adiabatic inversion of a two-level system by phase-
734 modulated pulses, *Phys Rev A (Coll Park)*, 32, 3435–3447,
735 <https://doi.org/10.1103/PhysRevA.32.3435>, 1985.

736 Brinkmann, A.: Introduction to average Hamiltonian theory. I. Basics, *Concepts in Magnetic*
737 *Resonance Part A*, 45A, e21414, <https://doi.org/10.1002/cmr.a.21414>, 2016.

738 Engelke, F.: Electromagnetic wave compression and radio frequency homogeneity in NMR solenoidal
739 coils: Computational approach, *Concepts Magn Reson*, 15, 129–155,
740 <https://doi.org/10.1002/cmr.10029>, 2002.

741 Gupta, R., Hou, G., Polenova, T., and Vega, A. J.: RF inhomogeneity and how it controls CPMAS, *Solid*
742 *State Nucl Magn Reson*, 72, 17–26, <https://doi.org/10.1016/j.ssnmr.2015.09.005>, 2015.

743 Hartmann, S. R. and Hahn, E. L.: Nuclear Double Resonance in the Rotating Frame, *Physical Review*,
744 128, 2042–2053, 1962.

745 [Hassan, A., Quinn, C. M., Struppe, J., Sergeev, I. V., Zhang, C., Guo, C., Runge, B., Theint, T., Dao, H.](https://doi.org/10.1016/j.jmr.2019.106680)
746 [H., Jaroniec, C. P., Berbon, M., Lends, A., Habenstein, B., Loquet, A., Kuemmerle, R., Perrone, B.,](https://doi.org/10.1016/j.jmr.2019.106680)
747 [Gronenborn, A. M., and Polenova, T.: Sensitivity boosts by the CPMAS CryoProbe for challenging](https://doi.org/10.1016/j.jmr.2019.106680)
748 [biological assemblies, *Journal of Magnetic Resonance*, 311, 106680,](https://doi.org/10.1016/j.jmr.2019.106680)
749 <https://doi.org/10.1016/j.jmr.2019.106680>, 2020.

750 Hediger, S., Meier, B. H., and Ernst, R. R.: ADIABATIC PASSAGE HARTMANN-HAHN CROSS-
751 POLARIZATION IN NMR UNDER MAGIC-ANGLE SAMPLE-SPINNING, *Chem Phys Lett*, 240, 449–456,
752 [https://doi.org/10.1016/0009-2614\(95\)00505-x](https://doi.org/10.1016/0009-2614(95)00505-x), 1995.

753 Hoult, D. I.: The principle of reciprocity in signal strength calculations - A mathematical guide,
754 *Concepts Magn Reson*, 12, 173–187, [https://doi.org/10.1002/1099-0534\(2000\)12:4<173::aid-](https://doi.org/10.1002/1099-0534(2000)12:4<173::aid-cmr1>3.0.co;2-q)
755 [cmr1>3.0.co;2-q](https://doi.org/10.1002/1099-0534(2000)12:4<173::aid-cmr1>3.0.co;2-q), 2000.

756 [Idziak, S. and Haeberlen, U.: DESIGN AND CONSTRUCTION OF A HIGH HOMOGENEITY RF COIL FOR](https://doi.org/10.1016/0022-2364(82)90058-0)
757 [SOLID-STATE MULTIPLE-PULSE NMR, *J Magn Reson*, 50, 281–288, https://doi.org/10.1016/0022-](https://doi.org/10.1016/0022-2364(82)90058-0)
758 [2364\(82\)90058-0](https://doi.org/10.1016/0022-2364(82)90058-0), 1982.

759 [Kelz, J. I., Kelly, J. E., and Martin, R. W.: 3D-printed dissolvable inserts for efficient and customizable](https://doi.org/10.1016/j.jmr.2019.06.008)
760 [fabrication of NMR transceiver coils, *Journal of Magnetic Resonance*, 305, 89–92,](https://doi.org/10.1016/j.jmr.2019.06.008)
761 <https://doi.org/10.1016/j.jmr.2019.06.008>, 2019.

762 [Krahn, A., Priller, U., Emsley, L., and Engelke, F.: Resonator with reduced sample heating and](https://doi.org/10.1016/j.jmr.2007.12.004)
763 [increased homogeneity for solid-state NMR, *J Magn Reson*, 191, 78–92,](https://doi.org/10.1016/j.jmr.2007.12.004)
764 <https://doi.org/10.1016/j.jmr.2007.12.004>, 2008.

765 [Laage, S., Sachleben, J. R., Steuernagel, S., Pierattelli, R., Pintacuda, G., and Emsley, L.: Fast](https://doi.org/10.1016/j.jmr.2008.10.019)
766 [acquisition of multi-dimensional spectra in solid-state NMR enabled by ultra-fast MAS, *J Magn Reson*,](https://doi.org/10.1016/j.jmr.2008.10.019)
767 [196, 133–141, https://doi.org/https://doi.org/10.1016/j.jmr.2008.10.019](https://doi.org/10.1016/j.jmr.2008.10.019), 2009.

768 Levitt, M. H.: Heteronuclear cross polarization in liquid-state nuclear magnetic resonance: Mismatch
769 compensation and relaxation behavior, *J Chem Phys*, 94, 30–38, <https://doi.org/10.1063/1.460398>,
770 1991.

771 Lowe, I. J.: Free Induction Decays of Rotating Solids, *Phys Rev Lett*, 2, 285–287,
772 <https://doi.org/10.1103/PhysRevLett.2.285>, 1959.

773 Marica, F. and Snider, R. F.: An analytical formulation of CPMAS, *Solid State Nucl Magn Reson*, 23,
774 28–49, [https://doi.org/10.1016/S0926-2040\(02\)00013-9](https://doi.org/10.1016/S0926-2040(02)00013-9), 2003.

775 [Marks, D. and Vega, S.: A Theory for Cross-Polarization NMR of Nonspinning and Spinning Samples, *J*](#)
776 [*Magn Reson A*, 118, 157–172, <https://doi.org/10.1006/jmra.1996.0024>, 1996.](#)

777 [Meier, B. H.: Cross polarization under fast magic angle spinning: thermodynamical considerations,](#)
778 [*Chem Phys Lett*, 188, 201–207, \[https://doi.org/10.1016/0009-2614\\(92\\)90009-C\]\(https://doi.org/10.1016/0009-2614\(92\)90009-C\), 1992.](#)

779 Metz, G., Wu, X. L., and Smith, S. O.: Ramped-amplitude cross-polarization in magic-angle-spinning
780 NMR, *J Magn Reson A*, 110, 219–227, <https://doi.org/10.1006/jmra.1994.1208>, 1994.

781 Paulson, E. K., Martin, R. W., and Zilm, K. W.: Cross polarization, radio frequency field homogeneity,
782 and circuit balancing in high field solid state NMR probes, *J Magn Reson*, 171, 314–323,
783 <https://doi.org/10.1016/j.jmr.2004.09.009>, 2004.

784 Peersen, O. B., Wu, X. L., and Smith, S. O.: Enhancement of CP-MAS Signals by Variable-Amplitude
785 Cross Polarization. Compensation for Inhomogeneous B1 Fields, *J Magn Reson A*, 106, 127–131,
786 <https://doi.org/http://dx.doi.org/10.1006/jmra.1994.1014>, 1994.

787 Pines, A., Gibby, M. G., and Waugh, J. S.: Proton-enhanced NMR of dilute spins in solids, *J Chem Phys*,
788 59, 569–590, <https://doi.org/10.1063/1.1680061>, 1973.

789 [Privalov, A. F., Dvinskikh, S. V, and Vieth, H. M.: Coil design for large-volume high-B-1 homogeneity](#)
790 [for solid-state NMR applications, *J Magn Reson A*, 123, 157–160,](#)
791 [<https://doi.org/10.1006/jmra.1996.0229>, 1996.](#)

792 Ray, S., Ladizhansky, V., and Vega, S.: Simulation of CPMAS signals at high spinning speeds, *J Magn*
793 *Reson*, 135, 427–434, <https://doi.org/10.1006/jmre.1998.1562>, 1998.

794 Rovnyak, D.: Tutorial on analytic theory for cross-polarization in solid state NMR, *Concepts in*
795 *Magnetic Resonance Part A*, 32A, 254–276, <https://doi.org/10.1002/cmr.a.20115>, 2008.

796 Schaefer, J.: Schaefer, Jacob: A Brief History of the Combination of Cross Polarization and Magic
797 Angle Spinning, in: *Encyclopedia of Magnetic Resonance*, John Wiley & Sons, Ltd, Chichester, UK,
798 <https://doi.org/10.1002/9780470034590.emrhp0161>, 2007.

799 Stejskal, E. O., Schaefer, J., and Waugh, J. S.: Magic-angle spinning and polarization transfer in
800 proton-enhanced NMR, *Journal of Magnetic Resonance (1969)*, 28, 105–112,
801 [https://doi.org/10.1016/0022-2364\(77\)90260-8](https://doi.org/10.1016/0022-2364(77)90260-8), 1977.

802 Tosner, Z., Andersen, R., Stevenss, B., Eden, M., Nielsen, N. C., Vosegaard, T., Stevensson, B., Eden,
803 M., Nielsen, N. C., and Vosegaard, T.: Computer-intensive simulation of solid-state NMR experiments
804 using SIMPSON, *J Magn Reson*, 246, 79–93, <https://doi.org/10.1016/j.jmr.2014.07.002>, 2014.

805 Tosner, Z., Porea, A., Struppe, J. O., Wegner, S., Engelke, F., Glaser, S. J., and Reif, B.: Radiofrequency
806 fields in MAS solid state NMR probes, *JOURNAL OF MAGNETIC RESONANCE*, 284, 20–32,
807 <https://doi.org/10.1016/j.jmr.2017.09.002>, 2017.

808 [Tošner, Z., Sarkar, R., Becker-Baldus, J., Glaubitz, C., Wegner, S., Engelke, F., Glaser, S. J., and Reif, B.:
809 Overcoming Volume Selectivity of Dipolar Recoupling in Biological Solid-State NMR Spectroscopy,
810 Angewandte Chemie - International Edition, 57, 14514–14518,
811 <https://doi.org/10.1002/anie.201805002>, 2018.](#)

812 Wu, X. L. and Zilm, K. W.: Cross Polarization with High-Speed Magic-Angle Spinning, *J Magn Reson A*,
813 104, 154–165, <https://doi.org/10.1006/jmra.1993.1203>, 1993.

814